Geochemical Studies of Earth Materials

by

John Ashby Mavrogenes

Dissertation submitted to the Faculty of the
Virginia Polytechnic Institute and State University
in partial fulfillment of the requirements for the degree of

DOCTOR OF PHILOSOPHY
in
Geological Sciences

APPROVED:

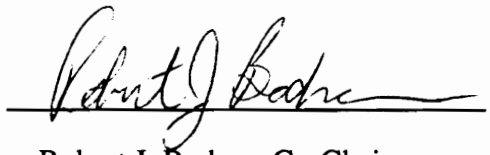

Robert J. Bodnar, Co-Chairman

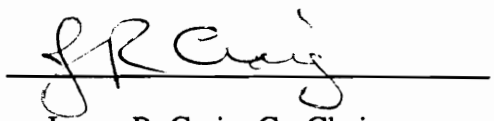

James R. Craig, Co-Chairman

David A. Hewitt

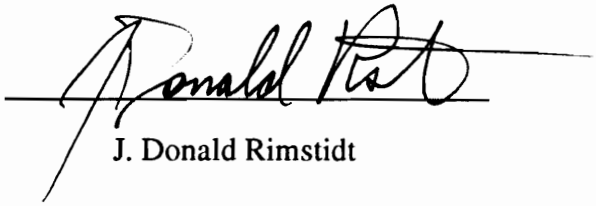

J. Donald Rimstidt

Michael F. Hochella

August, 1994
Blacksburg, Virginia

ABSTRACT

Natural chalcopyrite-bearing fluid inclusions from the Red Mountain, Arizona, porphyry copper prospect have been used to experimentally document the movement of hydrogen into and out of fluid inclusions in quartz. Chalcopyrite daughter minerals in inclusions do not dissolve during heating studies of "as collected" quartz vein material. However, after the samples were held at an elevated (but unknown) hydrogen pressure in a cold-seal-type pressure vessel at 600°C and 2.5 kbars for seven days, chalcopyrite daughter crystals dissolve easily and completely during subsequent heating in the fluid inclusion stage. The presence of hydrogen in the re-equilibrated inclusions was confirmed by both Raman microprobe and quadrupole mass spectrometric analyses of the inclusions. Repeated heating of re-equilibrated inclusions to measure the dissolution temperature of chalcopyrite (Tm Cpy) results in a considerably higher Tm Cpy during each successive run until, eventually, the chalcopyrite no longer dissolves when heated to the upper limit of the heating stage. This behavior is interpreted to indicate that hydrogen which had diffused into inclusions during re-equilibration experiments diffused out of the inclusions during microthermometric analyses.

The dissolution of chalcopyrite following re-equilibration and its failure to dissolve before re-equilibration are consistent with proposed solubility models for chalcopyrite in aqueous solutions. The rapid movement of hydrogen into inclusions is also consistent with experimentally determined diffusion rates for hydrogen through quartz. These results reinforce conclusions reached by earlier workers who suggested that the failure of some fluid inclusion daughter minerals to dissolve during heating is a result of hydrogen loss. These results also support earlier workers who have suggested that unexpectedly

low δD values obtained from inclusion fluids were produced by the preferential movement of hydrogen (relative to deuterium) into fluid inclusions.

Synchrotron X-ray Fluorescence (SXRF) analysis is a non-destructive analytical technique that provides compositional information for single fluid inclusions. Quantitative analyses of metals in individual synthetic fluid inclusions were carried out in order to gain an understanding of the accuracy, precision and detection limits of this technique, as well as the optimal shapes, sizes and geometries required for reliable fluid inclusion analysis.

Aqueous fluid inclusions containing known concentrations of $SrCl_2$ were synthesized for the development and the standardization of this technique. Strontium chloride was selected because it is highly soluble, its freezing-point depression is well known (allowing us to confirm the inclusion composition through freezing studies) and the energetic Sr X-rays are only mildly attenuated by quartz. SXRF analyses were performed on beam line X26A of the National Synchrotron Light Source (NSLS) at Brookhaven National Laboratory using an 8 x 12 μm "white" X-ray beam. The analytical volume was calculated based on known beam dimensions and fluid inclusion geometry determined using a modified spindle stage. Elemental concentrations were determined by ratioing the Sr counts from an inclusion to the counts obtained from capillaries of known diameter containing similar solutions.

Numerous inclusions from five different samples, each with a different Sr concentration, were analyzed. Within a single population the mean is very close to the correct composition, but the precision is poor, with standard deviations from 10-39% of the mean. Errors in determining the inclusion geometry produce the largest uncertainty in inclusion analysis thereby resulting in poor precision. This requires that numerous inclusions within one population be analyzed and averaged to obtain an accurate metal concentration for that population.

The Texaco gasification system developed at the Monte Bello pilot plant efficiently burns petroleum-coke thereby producing syn-gas and electricity. This system produces more electricity than conventional burners, yet the only by-products are pharmaceutical grade sulfur and V-rich slag. Vanadium is known to exist in multiple valence states in compounds which possess a wide range of melting points and physical properties. Consequently, it becomes important to carefully regulate oxygen fugacity throughout the system in order to control vanadium valence state. Vanadium phase equilibria is presently poorly understood, in large part because of the multiple oxidation states of vanadium (-1, 0, +2, +3, +4, and +5) and the difficulty of unequivocally identifying the valence state(s) in many compounds. However, V valence in multi-element phases (especially phases containing other elements of variable valence) cannot be resolved by microprobe analysis alone. Petroleum-coke gasification slags collected from within the gasifier under different oxidation conditions were studied by electron microprobe analysis (EMPA), X-ray diffraction (XRD), X-ray photoelectron spectroscopy (XPS) and Raman spectroscopy. Raman spectrometry in conjunction with microprobe analysis was found to resolve the valence of vanadium in the phases of these slags. Gasifier slag samples are, however, much more complicated. Oxidized samples contain: fine grained (Ca, Mg, Fe, V) oxide matrix of variable composition, (Fe, V, Ni) spinel, (Fe, Al, V, Ni, Mg) spinel, V_2O_5 laths, Al-Si glass blebs and Ni sulfides. Reduced samples contain: crystalline Ca-silicate matrix, subhedral to euhedral (V, Fe, Mg, Al) spinel, subhedral VO_2, Fe and Fe-Ni sulfides, Fe-Ni alloys, and complex Ca-oxide matrix. The different spinel assemblages, the characteristic V-oxides and the distinctly different character of the matrices makes the oxidized and reduced slags readily discernible.

ACKNOWLEDGMENTS

The research presented in Chapters two and three could not have been accomplished without the funding and guidance of Robert J. Bodnar, a great advisor and friend. Additional thanks go to Don Rimstidt, Mark Williamson, John Costain, Charlie Oakes, I-Ming Chou, Ian Samson and Anthony Williams-Jones for their contributions on hydrogen diffusion and chalcopyrite solubility (Chapter 2). The Synchrotron X-ray fluorescence analysis of fluid inclusions project (Chapter 3) could not have been completed without the assistance of the Brookhaven folks (Mark Rivers, Steve Sutton and Sasa Bajt) as well as Alan Anderson. The work on the Texaco petroleum-coke gasification slags (Chapter 4) was carried out in collaboration with James R. Craig. Texaco is thanked for supplying samples and a year of support. Also, Mike Hochella and Dave Hewitt should be thanked for serving on my committee and for teaching excellent classes on thermodynamics and surface chemistry. I feel privileged to have been associated with such a fine group of graduate students. And of course, many thanks to the wonderful geology department staff for being so helpful and friendly (even Karen Hunt).

TABLE OF CONTENTS

LIST OF FIGURES

LIST OF TABLES

Chapter 1: Introduction

The following is a collection of three diverse geochemical studies of natural and synthetic materials. Although these three papers are not directly related, they all share the common theme of micro-analysis of metal concentrations and the estimation of the oxidation state attending processes at elevated temperatures and pressures.

In Chapter 2 the affects of varying fO_2 on the solubility of chalcopyrite ($CuFeS_2$) contained in natural fluid inclusions from porphyry copper deposits is discussed. Hydrogen diffusion into and out of fluid inclusions in quartz is shown to occur rapidly at elevated temperatures. As hydrogen diffuses out of fluid inclusions (down concentration gradients) the solubility of chalcopyrite decreases until chalcopyrite crystals contained in fluid inclusions will not dissolve when heated in the laboratory. By experimentally forcing hydrogen back into these same inclusions, chalcopyrite can be dissolved during heating. Thus, although no data exist on the solubility of chalcopyrite at elevated temperatures and pressures, this study documented that chalcopyrite solubility increases dramatically at high fH_2. Furthermore, the results of this study suggest that hydrogen diffusion may significantly modify H/D ratios of inclusion fluids, casting considerable doubt on conclusions based solely upon isotopic analysis of fluids extracted from fluid inclusions.

Fluid inclusions containing large daughter crystals obviously trapped extremely metal-rich fluids, however, in most ore deposits metal concentrations in the ore forming fluid were not high enough to precipitate a solid phase upon cooling. In these cases, an analytical technique that enables analysis of cation abundances in fluid inclusions may hold the key to unraveling the chemical history of hydrothermal systems by fingerprinting the ore forming fluid pathways. Synchrotron X-ray fluorescence (SXRF)

analysis of fluid inclusions offers geochemists the hope of deriving such data. SXRF may not only provide the source and pathways of mineralizing solutions, but may, eventually, provide information on metal complexation in these systems (through the use of X-ray absorption studies). Previous workers determined fluid inclusion compositions by assuming ideal inclusion geometries. However, quantitative analyses of metal concentrations in fluid inclusions are only possible if fluid inclusion geometries are very well known, not estimated. In Chapter 3 the results of SXRF analyses of $SrCl_2$ - bearing synthetic fluid inclusions and the uncertainties involved with these analyses are presented. Now that the reliability of SXRF analyses of individual fluid inclusions is known, more applications to natural systems should be forthcoming.

The Texaco gasification process efficiently converts waste material into energy. In petroleum-coke gasifiers the oxidation state of vanadium (a major component) affects the operation of the system. Oxidized vanadium remains molten during operation, while reduced vanadium species crystallize, thereby halting proper flow-through of material within the gasifier. Valence determinations of vanadium in slags produced by this process may provide information on the conditions within the gasifier. This information should assist the Texaco engineers in improving the design and operation of such systems. However, unequivocal identification of the valence state(s) of vanadium in many compounds is difficult because of its multiple oxidation states (-1, 0, +2, +3, +4, and +5). In complex phases containing more than one element of variable valence (V and Fe) the valence of vanadium cannot be determined by electron microprobe analyses alone. The results of this study of petroleum-coke gasification slags, presented in Chapter 4, show that laser Raman analysis in tandem with electron microprobe analyses can determine the valence state of vanadium in complex phases.

Chapter 2: Hydrogen movement into and out of fluid inclusions in quartz: Experimental evidence and geologic implications

ABSTRACT

Natural chalcopyrite-bearing fluid inclusions from the Red Mountain, Arizona, porphyry copper prospect have been used to experimentally document the movement of hydrogen into and out of fluid inclusions in quartz. Chalcopyrite daughter minerals in inclusions do not dissolve during heating studies of "as collected" quartz vein material. However, after the samples were held at an elevated (but unknown) hydrogen pressure in a cold-seal-type pressure vessel at 600°C and 2.5 kbars for seven days, chalcopyrite daughter crystals dissolve easily and completely during subsequent heating in the fluid inclusion stage. The presence of hydrogen in the re-equilibrated inclusions was confirmed by both Raman microprobe and quadrupole mass spectrometric analyses of the inclusions. Repeated heating of re-equilibrated inclusions to measure the dissolution temperature of chalcopyrite (Tm Cpy) results in a considerably higher Tm Cpy during each successive run until, eventually, the chalcopyrite no longer dissolves when heated to the upper limit of the heating stage. This behavior is interpreted to indicate that hydrogen which had diffused into inclusions during re-equilibration experiments diffused out of the inclusions during microthermometric analyses.

The dissolution of chalcopyrite following re-equilibration and its failure to dissolve before re-equilibration are consistent with proposed solubility models for chalcopyrite in aqueous solutions. The rapid movement of hydrogen into inclusions is also consistent

with experimentally determined diffusion rates for hydrogen through quartz. These results reinforce conclusions reached by earlier workers who suggested that the failure of some fluid inclusion daughter minerals to dissolve during heating is a result of hydrogen loss. These results also support earlier workers who have suggested that unexpectedly low δD values obtained from inclusion fluids were produced by the preferential movement of hydrogen (relative to deuterium) into fluid inclusions. Finally, these results suggest that f_{O_2} conditions inferred from Raman or other microanalytical data obtained from fluid inclusions *may* not represent f_{O_2} conditions present at the time of trapping.

INTRODUCTION

One of the basic assumptions of fluid inclusion research is that nothing is added to, or lost from, inclusions after trapping. ROEDDER and SKINNER (1968) documented that major fluid components do not *normally* leak into or out of fluid inclusions during laboratory analysis. More recent studies have shown that water, in particular, may move through inclusion walls relatively easily in high-grade metamorphic environments (BAKKER and JANSEN, 1990; HOLLISTER, 1990). Compared to major components, it is generally accepted that hydrogen can, and probably does, leak from inclusions under certain conditions. Furthermore, ROEDDER (1984) suggested that hydrogen diffusion into or out of fluid inclusions may significantly change the Eh of the inclusion fluid and thereby change the solubility of included phases.

HALL and BODNAR (1990) quantitatively evaluated the effect of varying f_{H_2} on CO_2/CH_4 ratios in inclusions, and suggested that the small amounts of methane reported in fluid inclusions in granulites might be the result of hydrogen diffusion into inclusions. Similarly, HALL (1989) and HALL et al. (1991) showed that both the chemical and isotopic compositions of inclusions in massive sulfide deposits at Ducktown, Tennessee,

are consistent with diffusion of hydrogen into inclusions trapped during peak metamorphic conditions. MORGAN et al. (1993) have documented hydrogen diffusion through quartz and olivine and have described the concomitant chemical modifications to the fluids. In addition to the effect of f_{H_2} on volatile speciation in inclusions, hydrogen loss has also been called upon to explain the observation that sulfides and other solid phases (presumed to be daughter minerals) in inclusions do not dissolve during heating, although this assumption has not been tested experimentally.

In this study, we examined the effect of varying hydrogen fugacity on the solubility of chalcopyrite daughter minerals in natural fluid inclusions. This was accomplished by experimentally reversing the hypothesized hydrogen loss process experienced by natural inclusions, to produce inclusions with detectable hydrogen and in which the chalcopyrite dissolve during heating. Inclusions to which hydrogen has been added are referred to as re-equilibrated in this paper. This does not, however, imply that re-equilibration has restored the inclusions to the original f_{H_2} of trapping, but rather that some unknown amount of H_2 has been added to the inclusion. Finally, we consider some of the many implications of hydrogen loss relative to interpretations of chemical and isotopic data obtained from fluid inclusion analyses.

BACKGROUND

Fluid inclusions containing opaque, triangularly-shaped solids (Fig. 2.1) interpreted to be chalcopyrite have been reported from porphyry-type ore deposits worldwide (c.f., NASH, 1976; BODNAR and BEANE, 1980; EASTOE, 1978; ETMINAN, 1978; SAWKINS and SCHERKENBACH, 1981; RAMBOZ, 1979). Although there is little doubt that this phase is chalcopyrite, based on Gandolfi X-ray analysis of extracted solids

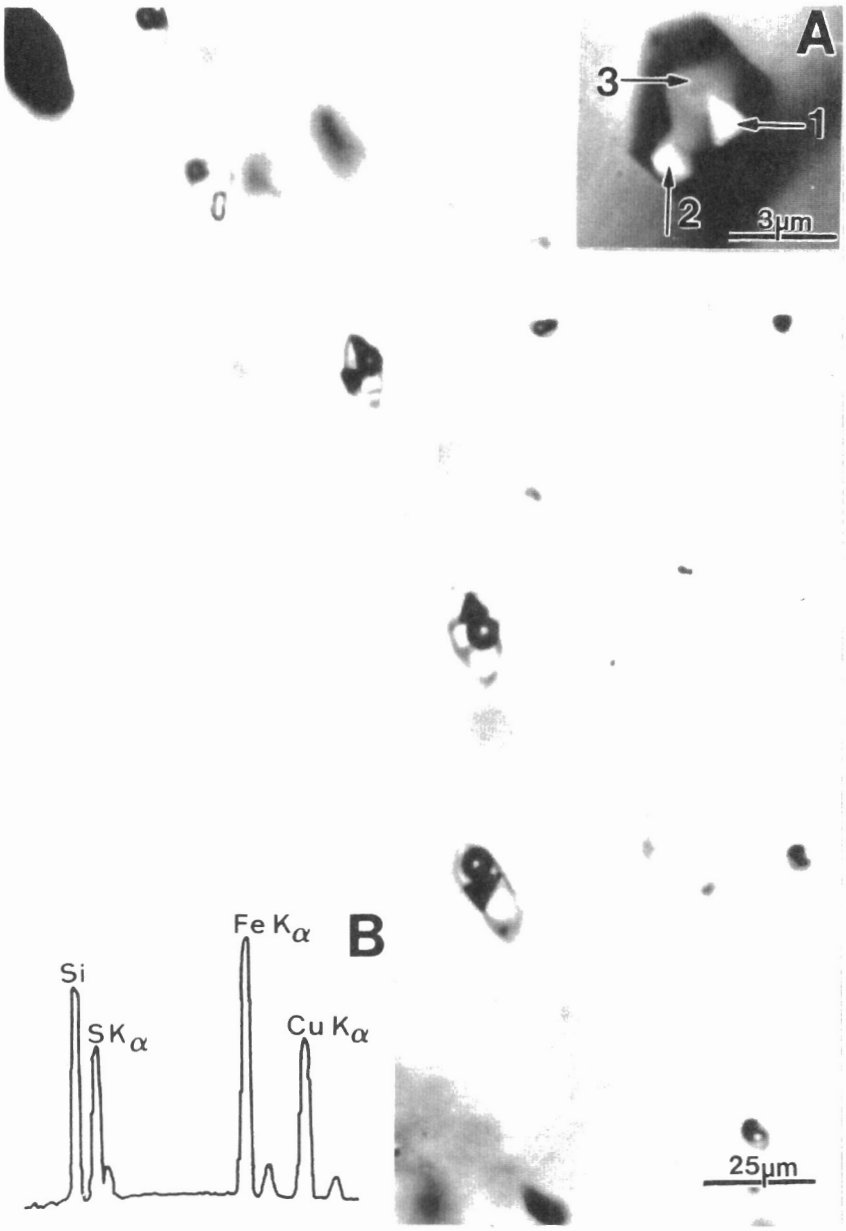

FIG. 2.1. Photomicrograph of a portion of a fluid inclusion trail in quartz from the Red Mountain, AZ, porphyry copper prospect. Each inclusion contains the same number of phases, including a triangular opaque chalcopyrite crystal, and in the same relative proportions. Photograph taken in plain transmitted light. Inset A: Backscatter SEM photomicrograph of an opened fluid inclusion from Red Mountain containing chalcopyrite (1), hematite (2) and halite (3). Inset B: Energy dispersive spectrum of the chalcopyrite grain in inset A.

(ZOLENSKY and BODNAR, 1982) and SEM analysis of opened inclusions (Fig. 2.1), many workers have questioned whether these chalcopyrite crystals were daughter minerals or trapped solids. This uncertainty resulted from the fact that, in some cases, the chalcopyrite was very large compared to the total inclusion volume and suggested copper (and iron and sulfur) contents in the original fluid that were much higher than thought to be probable or possible (on the order of a few weight percent copper). This uncertainty was heightened by the fact that the chalcopyrite crystal was never observed to dissolve, even partially, during microthermometric analysis of the inclusions.

Careful petrographic studies by numerous workers have shown that, at least in some cases, the chalcopyrite phase is a true daughter mineral, as evidenced by trails or planes of secondary inclusions in which each inclusion contains the same number of phases (including chalcopyrite) and in the same volume proportions (Fig. 2.1). Such fortuitous accidental trapping of solids is statistically improbable. The large size of the chalcopyrite phases, and the inferred very high copper solubilities in the inclusion fluid, have recently been shown to be consistent with copper solubilities determined from synthetic fluid inclusion studies (MAVROGENES et al., 1992).

Results of studies described earlier prove that the triangular, opaque solids in fluid inclusions from porphyry copper and related deposits are, indeed, chalcopyrite. Moreover, it is now clear that many of the chalcopyrite crystals are true daughter minerals and that the size of the chalcopyrite crystals is consistent with its expected solubility at magmatic hydrothermal conditions. The question that arises, then, is as follows: Why does chalcopyrite not dissolve when heated? Two explanations have been offered to explain this behavior. Some researchers have suggested that the kinetics are such that no appreciable solubility is observed over the duration of a normal heating experiment, and others have suggested that the chemistry in the inclusion fluid has changed since trapping owing to diffusive loss of hydrogen. The suggestion that the

failure of chalcopyrite to dissolve is a result of sluggish dissolution kinetics can be eliminated because of observations made by STERNER and BODNAR (1984, p. 2665) that chalcopyrite daughter minerals in synthetic fluid inclusions dissolve easily and completely during heating in the fluid inclusion stage. This leaves hydrogen loss as the only untested explanation for the failure of chalcopyrite to dissolve in natural inclusions.

EXPERIMENTAL PROCEDURE

In this study our goal was to experimentally test the effect of hydrogen pressure on the solubility of sulfide daughter minerals. This was accomplished using quartz containing chalcopyrite-bearing inclusions from the Red Mountain, Arizona, porphyry copper deposit. Previous studies of these same samples proved that the chalcopyrite crystals do not dissolve when the inclusions are heated (BODNAR and BEANE, 1980), and petrographic observations indicate that the chalcopyrite is a true daughter mineral (Fig. 2.1). We assumed that it would be necessary to heat the inclusions to a temperature approximately equal to their trapping temperature in order to affect total dissolution of the chalcopyrite. This, of course, means that the pressure in the inclusions at the dissolution temperature would equal the trapping pressure. Because fluid inclusions decrepitate when the internal pressure becomes too high, we selected inclusions that formed at low pressures. The Red Mountain samples have been shown to have formed at shallow depths (BODNAR and BEANE, 1980), and could probably be heated to their formation temperature without decrepitating.

Several doubly polished plates of a single quartz vein from Red Mountain were prepared and examined petrographically. The quartz plates were several hundred micrometers thick, but only those inclusions that were within approximately 20

micrometers of the sample surface were studied for reasons described below. A few representative inclusions in each sample were heated to 700°C to confirm that the chalcopyrite did not dissolve. The polished plates were then broken into smaller pieces for re-equilibration experiments, and some were set aside as control samples.

To reverse the hydrogen loss that occurred as the fluid inclusion-bearing quartz cooled in the presence of oxygenated meteoric waters during uplift and erosion of the Red Mountain deposit, the quartz was re-equilibrated at high hydrogen pressure at elevated temperatures and pressures. Samples of fluid inclusion-bearing quartz were placed in a 3 mm diameter platinum capsule containing water. The platinum capsule was sealed with an arc welder and sealed inside a gold capsule containing water and CrN (Fig. 2.2). The double capsule was then placed into a cold-seal-type pressure vessel and held at 2.5 kbars and 600°C for seven days. Microthermometric analysis (before re-equilibration) of the chalcopyrite-bearing inclusions from this sample indicated a salinity of about 55 wt.% NaCl and a liquid-vapor homogenization temperature [Th (L-V)] of 450-500°C. The experimental conditions were chosen to lie along the 55 wt.% NaCl isochore for a Th (L-V) of 475°C so that the internal inclusion pressure and the confining pressure would be approximately equal, thereby minimizing the possibility of decrepitation and/or leakage during the re-equilibration process.

When the capsule is heated, the CrN reacts with water to form chromium oxides, NH_3, N_2 and H_2 gas. According to I-Ming Chou (pers. commun., 1991), the CrN breakdown reaction produces more hydrogen per mole of starting material than any other commonly available compound suitable for use in hydrothermal experiments, thus generating a high (but unknown) hydrogen pressure outside the platinum capsule containing the inclusion-bearing quartz. Initially, most of the hydrogen produced by the breakdown of CrN is driven into the inner platinum capsule because hydrogen diffusion through platinum is much faster than through gold (Chou, 1987). The fluid inclusion-

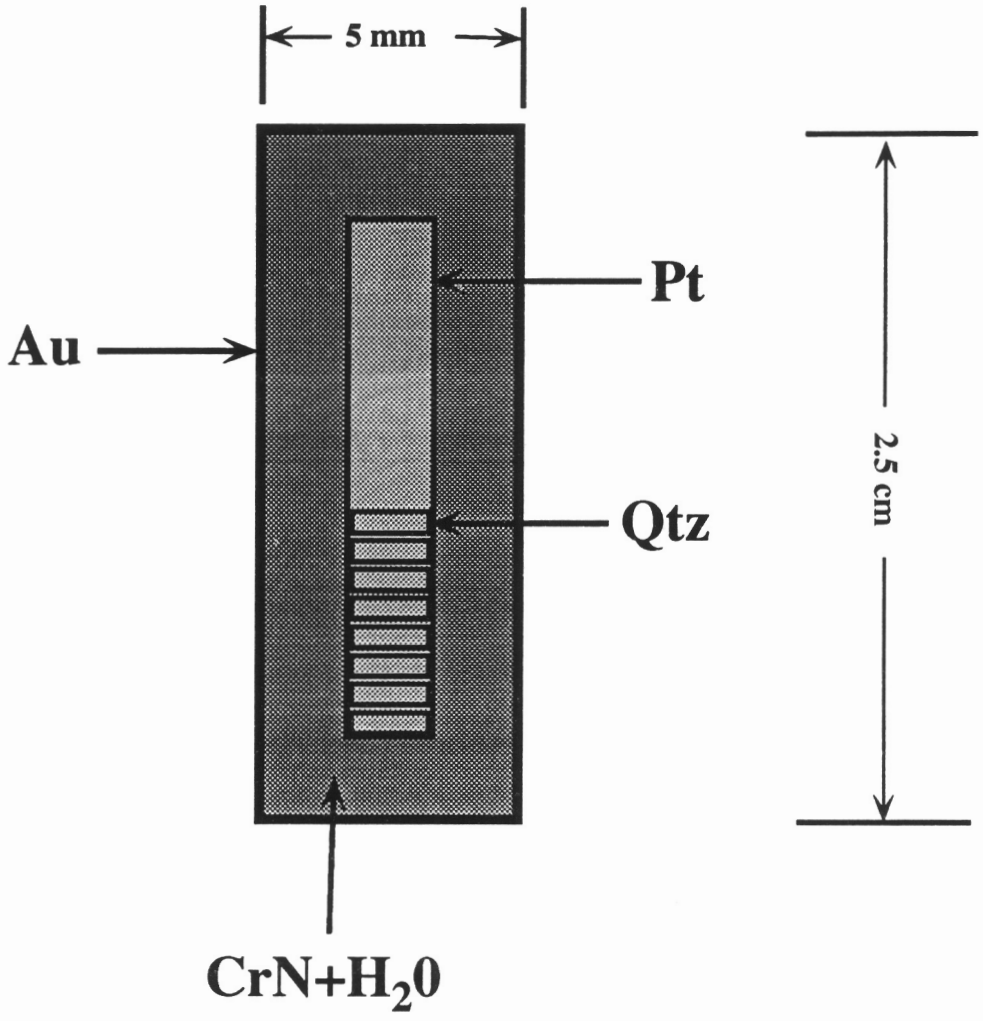

FIG. 2.2. Experimental design used for re-equilibration of natural chalcopyrite-bearing fluid inclusions. "Pt" and "Au" represent the inner platinum and outer gold capsules, respectively. "Qtz" represents the chalcopyrite-bearing quartz disks and "CrN + H_2O" represents the chromium nitride plus water used as starting materials to generate hydrogen at experimental conditions.

bearing quartz in the platinum capsule was thus exposed to a high hydrogen pressure for the duration of the run and this hydrogen, in turn, diffused through the quartz and into the inclusions.

At the end of the run, the sample was quenched and removed from the pressure vessel. The double-capsule was dried and weighed to verify that the gold capsule had not leaked. The gold capsule was then opened and the platinum capsule removed. The gold capsule was "puffed" at the end of a run, indicating an internal pressure above one atmosphere. A strong smell of ammonia was detected when the gold capsule was pierced, indicating that the source for the hydrogen was not completely exhausted during the experiment, thereby ensuring a high hydrogen pressure in the gold capsule for the duration of the experiment. Finally, the sample was removed from the platinum capsule and analyzed using various techniques described below.

RESULTS AND DISCUSSION

Diffusion of hydrogen into the inclusions during the re-equilibration experiments has been documented by several techniques. Raman microprobe analyses of all shallow (< 20 micrometers) re-equilibrated inclusions in quartz showed detectable hydrogen, as evidenced by a distinct peak at approximately 587 wavenumbers (Fig. 2.3). None of the chalcopyrite-bearing inclusions in the control samples that had not been re-equilibrated showed a detectable peak in this region. Based on experiments with a gas pressure cell (CHOU et. al., 1990) and on discussions with J. D. Pasteris (pers. commun., 1992) the minimum detection limit for hydrogen with the Raman microprobe is about 3 bars in the region 4150-4190 wave numbers, but in the 570 wavenumber region, detection limits appear to be as low as 1 bar. Failure to detect hydrogen in deeper inclusions is due to a

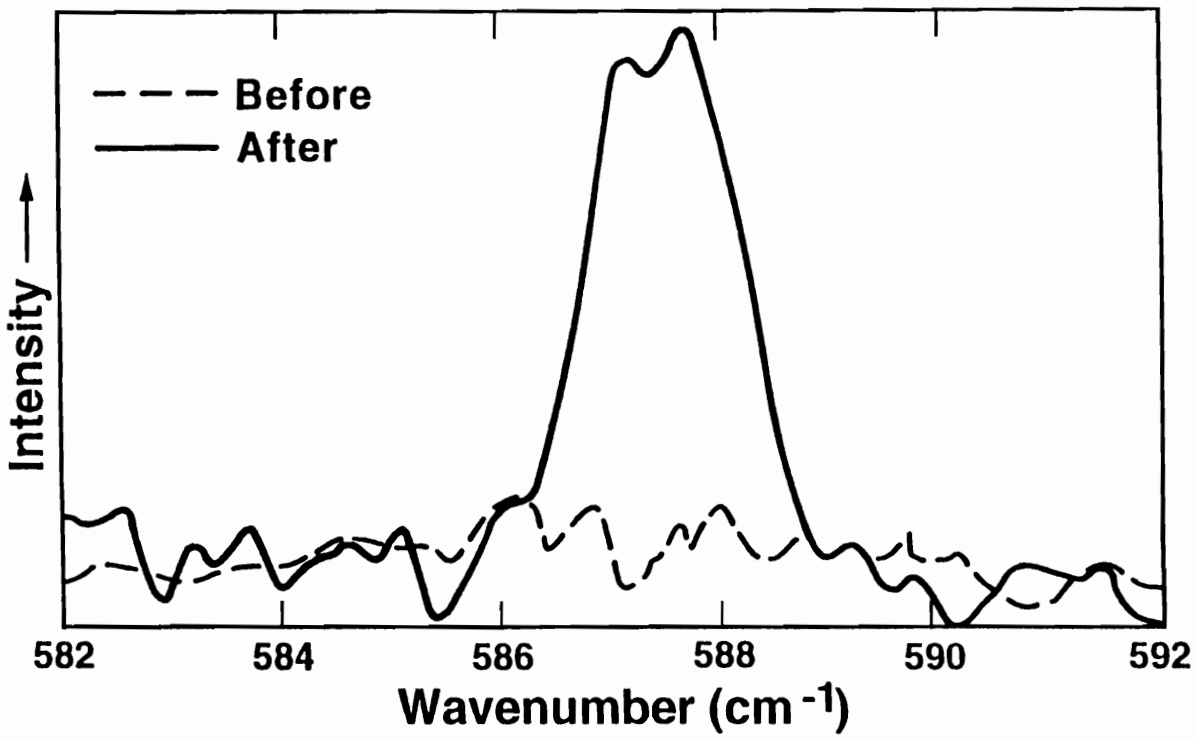

FIG. 2.3. Raman spectra of natural chalcopyrite-bearing fluid inclusions before and after re-equilibration. Dashed spectrum is before re-equilibration and the solid line is spectrum after being re-equilibrated at 600°C and 2.5 kbars for seven days. Both spectra were collected using 200 micrometer slit widths, .1 wavenumber step size, and 8 sec counting times.

combination of two factors; attenuation of the Raman scattered energy by the quartz host, and the decrease of hydrogen in re-equilibrated inclusions from Red Mountain and its absence from control sample inclusions was confirmed by quadrupole mass spectrometric analyses (J. Graney and S, Kesler, pers. commun., 1992).

The effect of the added hydrogen on the solubility of chalcopyrite was documented by results of heating runs on re-equilibrated inclusions. As mentioned above, the chalcopyrite crystals in "as collected", i.e, non-re-equilibrated or control inclusions, do not dissolve detectably during heating to temperatures of 700°C. However, microthermometric analysis of the re-equilibrated inclusions reveals that the chalcopyrite daughter crystals dissolve rapidly and completely when heated (Fig. 2.4). Note that only the smallest fluid inclusions could be heated to temperatures high enough for the dissolution of the chalcopyrite to be complete. Larger fluid inclusions decrepitated as a result of the high internal pressures generated during heating, as described by BODNAR et al. (1989). Thus, it was difficult to obtain high quality photographic evidence for chalcopyrite dissolution because only inclusions less than about 8-10 micrometers could be heated to the temperature of complete chalcopyrite dissolution and the largest size of the chalcopyrite in these inclusions was less than about 1-2 micrometers.

The failure of chalcopyrite in natural inclusions to dissolve when heated in the laboratory is consistent with the T-f_{H_2}-m_{Cu} relationships shown on Fig. 2.5. Copper solubility is relatively high in the magmatic/hydrothermal fluids originally trapped at high temperature and relatively high f_{H_2} (point A, Fig. 2.5). During and after cooling from trapping conditions, f_{H_2} decreases owing to diffusion of hydrogen out of the inclusion to produce a low f_{H_2} inclusion at room temperature (path A $\rightarrow$ B, Fig. 2.5). When this same inclusion is reheated in the laboratory, the solubility of chalcopyrite increases insignificantly as the inclusion follows an increasing temperature path at low f_{H_2} (path B

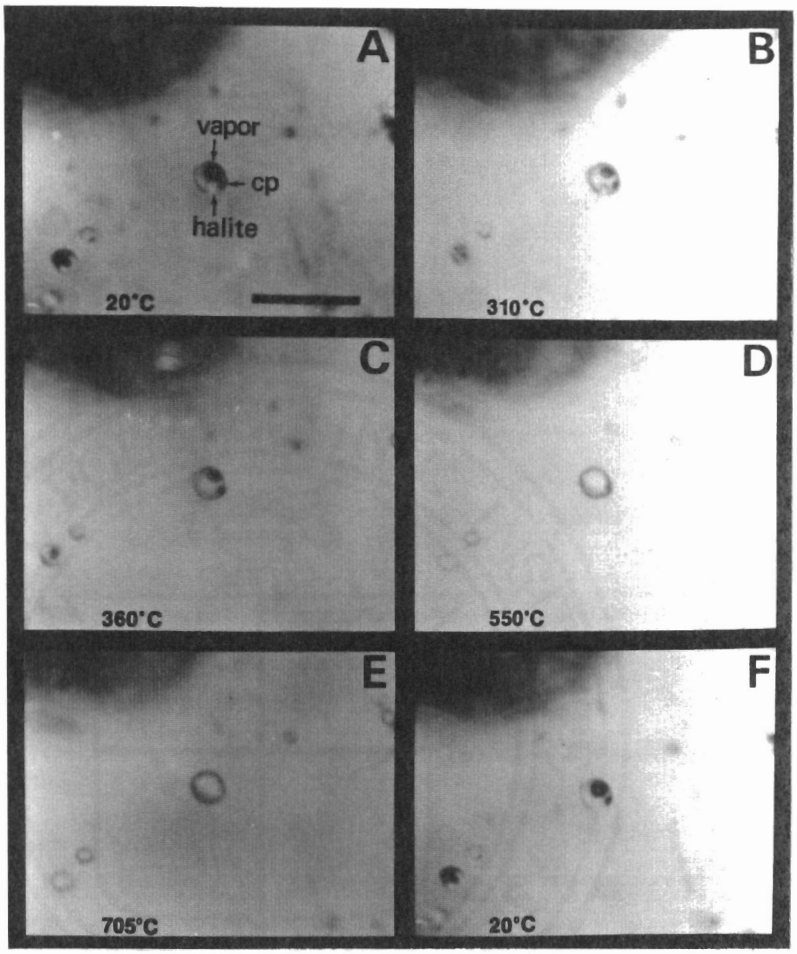

FIG. 2.4. Photomicrographs showing the dissolution of halite and chalcopyrite (cp) in a natural fluid inclusion following re-equilibration at 600°C and 2.5 kbars. Before re-equilibration, the chalcopyrite exhibited no discernible change when heated to the same temperatures. Note that smaller inclusions in the lower left portion of the photographs also contain chalcopyrite daughter minerals that dissolve during heating. The scale bar equals 20 micrometers.

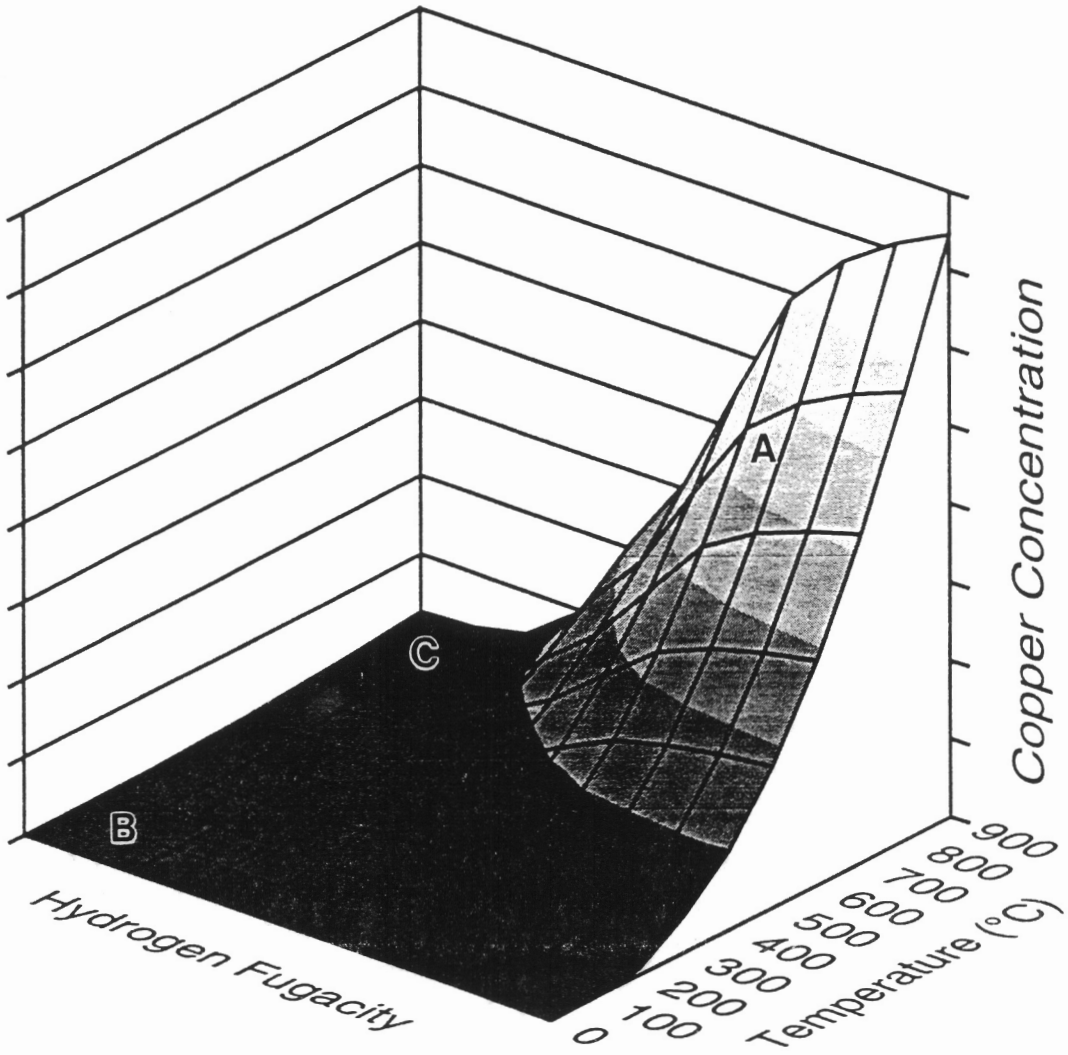

FIG. 2.5. Schematic representation of the effect of hydrogen pressure (bars) and temperature (°C) on chalcopyrite solubility, represented by Cu solubility. Point "A" represents assumed initial formation conditions for chalcopyrite-bearing fluid inclusions in the porphyry copper environment; point "B" represents conditions in the inclusion after cooling, uplift, and loss of hydrogen from the inclusion; path "B ⇒ C" represents path followed by natural chalcopyrite-bearing inclusions when heated in the laboratory before re-equilibration.

$\rightarrow$ C, Fig. 2.5) owing to the much lower f_{H_2} today compared to that originally in the inclusion.

In this study we have not attempted to rigorously evaluate the mechanistic changes responsible for the increased solubility of chalcopyrite as hydrogen pressure is increased. We do not have sufficient information on the compositions of the natural fluid inclusions used in this study, nor do we know the exact value of the hydrogen pressure in the inclusions following re-equilibration.

These uncertainties are being addressed in an ongoing study using synthetic fluid inclusions to measure the solubility of chalcopyrite and other base metal sulfides at elevated temperatures and carefully controlled solution parameters (pH, fO_2, fS_2, etc.). For these reasons, Fig. 2.5 has been constructed to depict the qualitative effect of hydrogen fugacity on chalcopyrite solubility. The relatively high solubilities (thousands of ppm) of chalcopyrite expected in high salinity (30-70 wt.% NaCl) fluids at high temperature and high f_{H_2} are confirmed by preliminary experiments on natural inclusions, as described below, and by recent solubility measurements using synthetic fluid inclusions (MAVROGENES et al., 1992).

The experiments described above represent the first documented case of a chalcopyrite daughter phase in a natural fluid inclusion dissolving during heating. These results, as well as evidence which shows that the phase is chalcopyrite and that chalcopyrite is in some cases a true daughter mineral, indicate high copper concentrations in ore-forming fluids in porphyry type deposits. It is important to note that the temperature of chalcopyrite dissolution measured in the re-equilibrated fluid inclusions should not be accepted as the temperature of chalcopyrite dissolution in the original fluid trapped in the inclusion. We have generated an artificially high hydrogen fugacity, probably much higher than that originally in the inclusion, and the dissolution temperature is dependent on the hydrogen pressure (as well as other solution properties,

such as pH). The goal of this study was simply to show that a chalcopyrite crystal which would not dissolve previously would dissolve after hydrogen was added to the inclusion. Thus, the copper content of the ore-forming fluid that one would obtain from analysis of the inclusion would be correct, but the temperature at which this amount of copper was soluble in the original ore-forming fluid is not necessarily the same as that at which the chalcopyrite dissolved in our experiments.

We have demonstrated that "large" (but unknown) amounts of hydrogen can move significant distances (hundreds of micrometers) through quartz in several days, but have not documented the mechanism of hydrogen movement. Hydrogen could move into the inclusions by bulk diffusion or it could move by dispersion or surface diffusion along very small, poorly healed fractures. We have described the movement of hydrogen as being diffusion controlled, but we have provided no proof to support this claim. Hydrogen could, of course, move much more rapidly by dispersion or surface diffusion along very small, poorly healed fractures. In order to determine whether our results are consistent with a diffusional mechanism for hydrogen transfer, we have compared our empirical observational data to published diffusion rates for hydrogen through quartz.

KATS et al. (1962) used spectrophotometry to determine the diffusion coefficient for hydrogen through quartz over the temperature range 400°-900°C. We have plotted their log D vs. 1/T (K) data in Fig. 6 and have fitted linear regressions to both the high temperature (β quartz) and low temperature (α quartz) segments. The low temperature segment was extrapolated down to 20°C (Fig. 2.6). The D value derived from those data is related to hydrogen pressure and depth within a quartz crystal by Fick's second law, as follows:

$$\frac{\partial^2 P}{\partial Z^2} = \frac{1}{D}\frac{\partial P}{\partial t} \qquad (2.1)$$

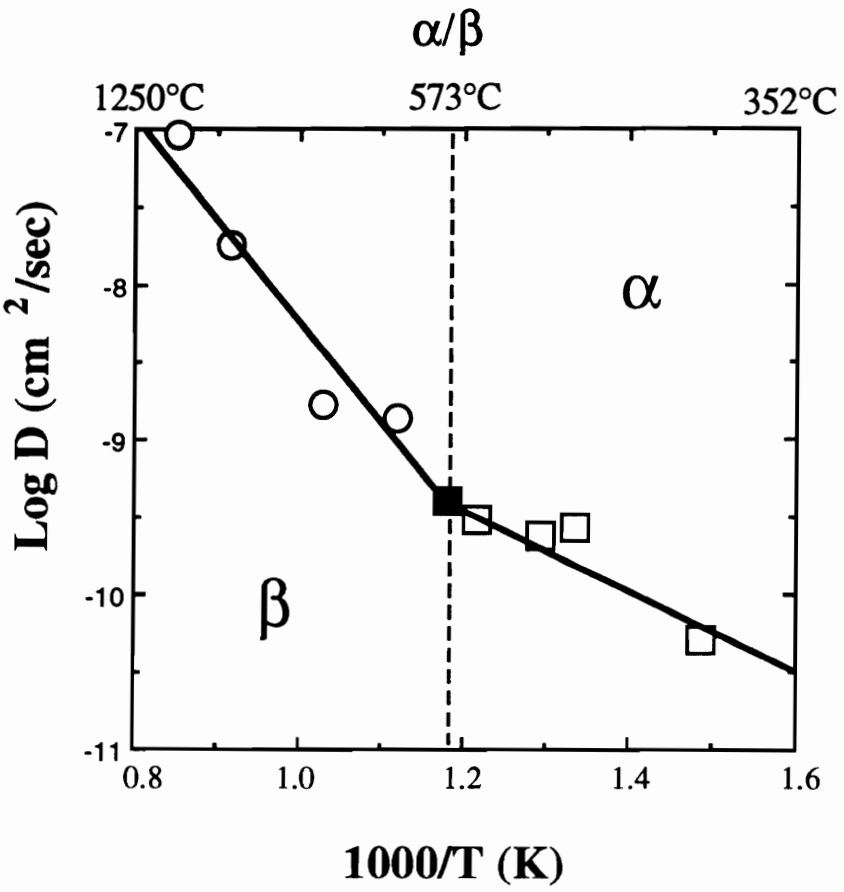

FIG. 2.6. Log D vs. 1/T data for diffusion of hydrogen through quartz from KATS et al. (1962). The lines represent simple linear least squares regression analyses of the data of KATS et al.(1962).

where t = time (seconds), P = pressure (bars), Z = depth (centimeters) and D = the diffusion coefficient ($cm^2 \bullet sec^{-1}$). A numerical solution to this second order differential equation, from a planar source, is given by HOWELS (1974), as:

$$P(Z,t) = P_o\left[1\text{-error function}\left(\frac{Z}{2((Dt)^{0.5})}\right)\right] \qquad (2.2)$$

where $P_o = H_2$ pressure (bars) at the crystal surface; $P = H_2$ pressure (bars) at depth Z; Z = depth (centimeters); t = time (seconds); D = the diffusion coefficient ($cm^2 \bullet sec^{-1}$). The time required for the interior H_2 pressure reached 95% of the H_2 pressure at the crystal surface was calculated for a variety of depths and temperatures (which is included in the D term). The results are shown in Fig. 2.7; data have been converted to micrometers and hours to facilitate comparison with our experimental measurements. Note that this model is only valid for diffusion of hydrogen *into* fluid inclusions in quartz, and should not be used to consider diffusion rates out of fluid inclusions because the equation describing diffusion from a point source (inclusion) is different than that presented above for diffusion from a plane. The amounts of time required to reach 95% equilibration shown on Fig. 2.7 and calculated from the data of KATS et al. (1962) agree remarkably well with our experiments. For example, shallow inclusions (<20 μm below the surface) contained detectable hydrogen after 170 ($10^{2.23}$) h at 600°C. Our calculated estimate for a 20 μm deep fluid inclusion at 600°C to reach 95% re-equilibration is 286 ($10^{2.46}$) h; and in 170 ($10^{2.23}$) h, an inclusion 16 μm below the surface would be 95% re-equilibrated. As shown on Fig. 2.7, the re-equilibration time increases significantly with decreasing temperature. A 20 μm deep fluid inclusion significantly would reach 95% re-

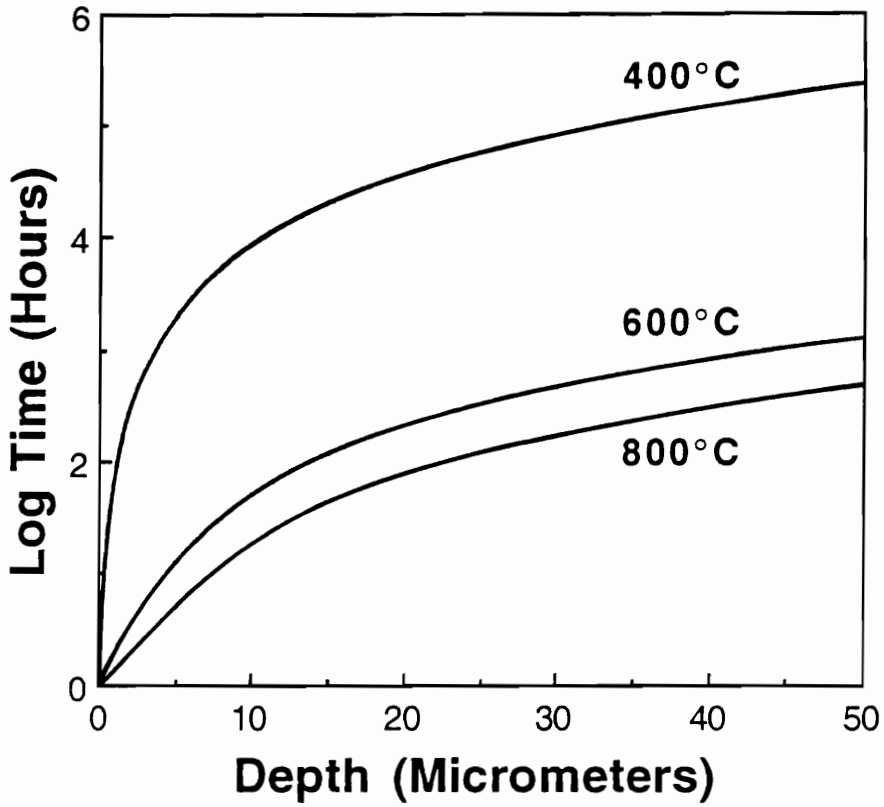

FIG. 2.7. Calculated time required to achieve 95% equilibration in hydrogen pressure inside and outside of fluid inclusions in quartz at the depths indicated.

equilibration at 400°C after 2138 ($10^{3.33}$) h, while the same inclusion at 800°C would require only 80 ($10^{1.9}$) h.

GEOLOGIC IMPLICATIONS

The major conclusion of this study is that fluid inclusions may gain or lose hydrogen when the hydrogen fugacity outside the inclusion differs from that inside. As a result, inclusion phases that contain elements (e.g. C, S, and many transition metals) that commonly exist in more than one valence state at redox conditions encountered in the Earth's crust are likely to change their speciation and chemistry. Often, fO_2 conditions associated with a given geologic process or environment are calculated from the phase assemblage present in inclusions. However, the assumption inherent in these calculations is that the phase assemblage in the inclusion today is representative of the fO_2 conditions at the time of trapping. Obviously, if loss or gain of hydrogen has occurred since the time of trapping, the calculated fO_2 may be significantly different than that at trapping. For example, HALL et al. (1991) reported that the CO_2/CH_4 ratios in fluid inclusions indicated fO_2 conditions that were in disagreement with those predicted by silicate and sulfide phase equilibria for the surrounding rocks. These workers interpreted this disagreement as the result of hydrogen diffusion into the inclusions following entrapment.

The basic assumption of fluid inclusion research tested in this study concerns the gain or loss of components by inclusions after entrapment. It is also assumed that inclusions trap a single, homogeneous phase and that multiple phases (liquid, vapor, solid) in inclusions today are normal consequence of equilibrium phase changes that occur during cooling form formation temperature to room temperature. This assumption

is generally considered valid if a group of coeval inclusions all contain the small phases in the same relative volume percentages and if the phases all homogenize at the same temperature. The failure of some solid phases to dissolve when heated has led some workers to suggest that these phases were trapped as solids and are not daughter minerals. In some cases petrographic evidence supports the interpretation that solids were trapped by the inclusions. However, in other cases the uniformity of phases and their relative proportions in a large number of coeval inclusions is positive proof that the solids are daughter minerals, even though these solids do not dissolve during heating. Thus, failure of the solids to dissolve in these inclusions is the result of violation of the first assumption concerning gain or loss of material and is not due to trapping of solids by the inclusion, which is related to the second assumption.

It is important to note that the vast majority of non-dissolving solid phases which have been identified contain one or more of the elements sulfur (base metal sulfides, anhydrite, gypsum), carbon (carbonates), or iron (pyrite, magnetite, hematite), each of which occurs in more than one valence state at fO_2 conditions commonly prevailing in hydrothermal systems. Thus, it is our recommendation that if a solid phase in an inclusion contains one of the elements listed above; and if a large number of coeval inclusions also contain this same phase and in the same relative proportions, the solid should be interpreted as a daughter mineral even though it may not dissolve during heating. An important related issue is that when calculating compositions of fluids in inclusions the material in the solid phase must be included to obtain an accurate representation of the fluid that was trapped. This also means that any bulk analysis of inclusions containing such solid phases must incorporate that material contained in the solid into the final determined composition. This becomes particularly true of analyses of fluid inclusions containing base metal sulfides, such as chalcopyrite, galena, sphalerite,

etc., if one is trying to determine the concentration of ore metals in the inclusion fluid from crushing or other bulk analysis techniques.

A final implication of the results of this study concerns isotopic analysis of inclusion fluids to determine the compositions of fluids to determine the compositions of fluids responsible for mineralization and alteration. The methodology generally employed when the inclusion host is quartz or some other oxygen-bearing phase is to measure the D/H ratio of inclusion fluids and then to calculate the $^{18}O/^{16}O$ ratio of the original fluid assuming some temperature and fractionation factor. However, if hydrogen has diffused into or out of inclusions, the D/H ratio of the inclusion may differ significantly from that of the fluid originally trapped because hydrogen will diffuse through the host mineral structure much faster than deuterium. Thus, if hydrogen has diffused into inclusions, one would expect anomalously light D/H values for the remaining inclusion fluid, whereas diffusion out of inclusions will result in anomalously heavy D/H values. HALL (1989) reported unexpectedly low D/H ratios, and unexpectedly large amounts of CH_4, in inclusions from the metamorphosed massive sulfide deposits at Ducktown, Tennessee. HALL (1989) estimated that these values indicated addition of approximately 20 mol% hydrogen via diffusion from the surroundings.

Our experimental results, combined with the calculated rates of diffusion described above, document the ease with which hydrogen can move into or out of inclusions in quartz. One could interpret these results to mean that all fluid inclusions should re-equilibrate to the surrounding fO_2 conditions. Moreover, because most samples studied are collected near the surface and have been exposed to near-surface oxidizing conditions for some (unknown) length of time, we should never expect to find inclusions with detectable hydrogen. This is obviously not the case, and the presence of significant amounts of hydrogen has been detected in natural fluid inclusions in quartz using Raman spectroscopy (DUBESSY et al., 1988). The presence of hydrogen in these inclusions

from Precambrian age rocks would appear, at first glance, to conflict with our diffusive model but, may actually provide evidence in support of our model. The hydrogen-bearing fluid inclusions described by DUBESSY et al. (1988) are from Precambrian uranium deposits (Oklo, Rabbit Lake and Cluff Lake), and these workers attribute the formation of the H_2 in these fluid inclusions to radiolysis. This ongoing process continuously generates hydrogen within the inclusions, thereby replacing any hydrogen that may have diffused out.

A second commonly reported occurrence of hydrogen-bearing inclusions is from alkalic intrusions such as those in Greenland (KONNERUP-MADSEN et al., 1985). However, KONNERUP-MADSEN et al. (1981) also reported the presence of significant amounts of hydrocarbons (50->90% of the gas phase) in inclusions from these intrusions. As with hydrogen-bearing inclusions in the uranium deposits, these inclusions contain a ready source of hydrogen from the breakdown of higher hydrocarbon components into lighter components with the release of hydrogen.

An additional factor which must be considered when evaluating whether or not a given inclusion or group of inclusions has maintained the original trapping fO_2 conditions is the post-entrapment history of the sample. Hydrogen will diffuse out of inclusions if the inclusion-bearing sample is exposed to fO_2 conditions significantly different than those in the inclusions. Moreover, because diffusion rates are very slow at low temperatures, a sample that is placed in an oxidizing environment at low temperatures will not readily lose hydrogen. Conversely, the presence of non-dissolving daughter minerals is a good indication that, not only has the sample been exposed to fO_2 conditions different from those of the fluid originally trapped, but that this exposure occurred at temperature/time conditions sufficient for significant amounts of hydrogen to diffuse. Thus, non-dissolving daughter minerals in fluid inclusions from the porphyry copper environment support the model which envisions an early, high temperature

magmatic/hydrothermal system with reducing ore-bearing solutions, followed by an influx of more oxidizing meteoric water. Convective flow of these fluids through the still-hot intrusive serves to bathe the entire system in oxidizing fluids and maintain the oxidizing solution at moderate temperatures (≤350° - 400°C) for several tens to hundreds of thousands of years (NORTON, 1982).

REFERENCES

BAKKER, R.J. and JANSEN, B.H. (1990) Preferential water leakage from fluid inclusions by means of mobile dislocations. *Nature*, **345**, 58-60.

BODNAR, R.J., and BEANE, R.E. (1980) Temporal and spatial variations in hydrothermal fluid characteristics during vein filling in pre-ore cover overlying deeply buried porphyry copper-type mineralization at Red Mountain, Arizona. *Econ. Geol.*, **75**, 876-893.

BODNAR, R.J., BINNS, P.R., and HALL, D.L. (1989) Synthetic fluid inclusions-VI. Quantitative evaluation of the decrepitation behaviour of fluid inclusions in quartz at one atmosphere confining pressure. *J. Met. Geol.*, **7**, 229-242.

CHOU, I-MING (1987) Oxygen buffer and hydrogen sensor techniques at elevated pressures and temperatures. In *Hydrothermal Experimental Techniques* (ed. G.C. Ulmer and H.L. Barnes), John Wiley & Sons, N.Y., pp. 61-99.

CHOU, I-MING, PASTERIS, J. D. and SEITZ, J. C. (1990) High density volatiles in the system C-O-H-N for the calibration of a laser Raman microprobe. *Geochim. Cosmochim. Acta*, **54**, 535-534.

DUBESSY, J., PAGEL, M., BENY, J.M., CHRISTENSEN, H., HICKEL, B., KOSZTOLANYI C., and POTY, B. (1988) Radiolysis evidenced by H_2-O_2 and H_2-bearing inclusions in three uranium deposits. *Geochim. Cosmochim. Acta*, **52**, 1155-1167.

EASTOE, C.J. (1978) A fluid inclusion study of the Panguna porphyry copper deposit, Bouganville, Papua New Guinea. *Econ. Geol.*, **73**, 721-748.

ETMINAN, H. (1978) Fluid inclusion studies of the porphyry copper ore bodies at Sar-Chesmeh, Darreh Zar and Mieduk (Kerman region, southeastern Iran) and porphyry copper discoveries at Songun, Gozan, and Kighal, Azarbyzan region (northwestern Iran): International Association on the Genesis of Ore Deposits, Fifth Symposium, Snowbird, Utah, Abstracts, p. 88.

HALL, D. L. (1989) Fluid evolution during metamorphism and uplift of the massive sulfide deposits at Ducktown, Tennessee, U.S.A. Unpub. Ph.D. Dissertation, Virginia Polytechnic Institute & State University, Blacksburg, VA 263 pp.

HALL, D. L. and BODNAR, R. J. (1990) Methane in fluid inclusions from granulites: A product of hydrogen diffusion? *Geochim. Cosmochim. Acta*, **54**, 641-651.

HALL, D. L., BODNAR, R. J. and CRAIG, J. R. (1991) Evidence for post entrapment diffusion of hydrogen into peak metamorphic fluid inclusions from the massive sulfide deposits at Ducktown, Tennessee. *Amer. Miner.*, **76**, 1344-1355.

HOLLISTER, L.S. (1990) Enrichment of CO_2 in fluid inclusions in quartz by removal of H_2O during crystal-plastic deformation. *J. Struct. Geol.*, **12**, 895-901.

HOWELS, D.A. (1974) The time for a significant change of pore pressure. *Geology*, **8**, 135-138.

KATS, A., HAVEN, Y. and STEVELS, J.M. (1962) Hydroxyl groups in alpha quartz. *Physics and Chemistry of Glasses*, **3**, no. 3, 69-75.

KONNERUP-MADSEN, J., ROSE-HANSEN, J. and LARSEN, E. (1981) Hydrocarbon gases associated with alkaline igneous activity: evidence from compositions of fluid inclusions. *Rapp. Gronlands goel. Unders.* **103**, 99-108.

KONNERUP-MADSEN, J., DUBESSY, J and ROSE-HANSEN, (1985) Combined Raman microprobe spectrometry and microthermometry of fluid inclusions in minerals from igneous rocks of the Gardar province (south Greenland). *Lithos*, **18**, 271-280.

MAVROGENES, J. A., WILLIAMSON, M. A. and BODNAR, R. J. (1992) Cu, Fe and S concentrations in magmatic/hydrothermal fluids: Evidence from natural and synthetic fluid inclusions.*Geol. Soc. Amer. Abstr. Prog.*, **24**, A-144.

MORGAN, G. B., CHOU, I-MING, PASTERIS, J. D., and OLSEN, S. N. (1993) Re-equilibration of CO_2 fluid inclusions at controlled hydrogen fugacities. *Journal of Metamorphic Geology* , **11**, 155-164.

NASH, T.J. (1976) Fluid-inclusion petrology - data from porphyry copper deposits and applications to exploration. *U. S. Geol. Surv. Prof. Paper 907-D*, 16 pp.

NORTON, D. L. (1982) Fluid and heat transport phenomena typical of copper-bearing pluton environments. In *Advances in Geology of the Porphyry Copper Deposits,* (ed. S. R. Titley), The University of Arizona Press, Tucson, AZ, p.59-72.

RAMBOZ, C. (1979) A fluid inclusion study of the copper mineralization in southwest Tintic district (Utah). *Bull. Mineral.*, **102**, p. 622-632.

ROEDDER, E. (1984) *Fluid inclusions,* Mineral. Soc. Amer. Reviews in Mineralogy: **12**, 644p.

ROEDDER, E., and SKINNER, B.J. (1968) Experimental evidence that fluid inclusions do not leak. *Econ. Geol.*, **63**, 715-730.

SAWKINS, F.J., and SCHERKENBACH, D.A. (1981) High copper content of fluid inclusions in quartz from northern Sonora: Implications for ore-genesis theory. *Geology*, **9**, 37-40.

STERNER, S. M. and BODNAR, R. J. (1984) Synthetic fluid inclusions in natural quartz. I. Compositional types synthesized and applications to experimental geochemistry. *Geochim. Cosmochim. Acta*, **48**, 2659-2668.

ZOLENSKY, M.E. and BODNAR, R.J. (1982) Identification of fluid inclusion daughter minerals using Gandolfi x-ray techniques. *Amer. Mineral.*, **67**, 137-141.

Chapter 3: Assessment of the Uncertainties and Limitations of Quantitative Elemental Analysis of Individual Fluid Inclusions using Synchrotron X-ray Fluorescence

ABSTRACT

Synchrotron X-ray Fluorescence (SXRF) analysis is a non-destructive analytical technique that provides compositional information for single fluid inclusions. Quantitative analyses of metals in individual synthetic fluid inclusions were carried out in order to gain an understanding of the accuracy, precision and detection limits of this technique, as well as the optimal shapes, sizes and geometries required for reliable fluid inclusion analysis.

Aqueous fluid inclusions containing known concentrations of $SrCl_2$ were synthesized for the development and the standardization of this technique. Strontium chloride was selected because it is highly soluble, its freezing-point depression is well known (allowing us to confirm the inclusion composition through freezing studies) and the energetic Sr X-rays are only mildly attenuated by quartz. To confirm the composition of the synthetic standards, solutions were measured before and after each hydrothermal run using Atomic Absorption Spectroscopy (AAS), and the freezing-point depression for each fluid inclusion was measured.

SXRF analyses were performed on beam line X26A of the National Synchrotron Light Source (NSLS) at Brookhaven National Laboratory using an 8 x 12 μm "white" X-ray beam. The analytical volume was calculated based on known beam dimensions and fluid inclusion geometry determined using a modified spindle stage. Elemental concentrations were determined by ratioing the Sr counts from an inclusion to the counts obtained from capillaries of known diameter containing similar solutions.

Numerous inclusions from five different samples, each with a different Sr concentration, were analyzed. Within a single population the mean is very close to the correct composition, but the precision is poor, with standard deviations from 10-39% of the mean. Errors in determining the inclusion geometry produce the largest uncertainty in inclusion analysis thereby resulting in poor precision. This requires that numerous inclusions within one population be analyzed and averaged to obtain an accurate metal concentration for that population. Additionally, selection of flat-lying, equant, regularly shaped inclusions in clear quartz will help to minimize errors resulting from poorly constrained inclusion geometries and high background levels if quantitative results are sought. The detection limit for Sr in synthetic fluid inclusions (typically 4-15 μm thick) is approximately 2,000 ppm Sr.

INTRODUCTION

In studies of hydrothermal ore deposits, one of the most often asked questions concerns the source(s) of ore metals and the concentrations of metals in ore-forming fluids. Theoretical calculations (HELGESON, 1992) and results of experimental studies (BARNES, 1979: KEPPLER and WYLLIE, 1991), as well as analyses of fluids from active geothermal systems (WEISSBERG et al., 1979), volcanoes (SYMONDS, 1992) and oil-field brines (CARPENTER et al., 1974) provide indirect answers to these questions. The most direct and convincing evidence, however, comes from the identification of fluid inclusions associated with mineralization and the analysis of these inclusions to determine the type and concentration of contained metals.

Numerous techniques, including electron microscopy of opened (HAYNES et al., 1988) and unopened fluid inclusions (e.g. MAASKANT, 1986), laser ablation and crushing ICP (see SHEPHARD et al., 1985), proton induced X-ray emission (PIXE) and gamma-ray emission (PIGE) spectroscopies (HORN et al., 1987; ANDERSON et al., 1989; HEINRICH et al., 1992) have been applied to determine metal contents of fluid inclusions. Although data provided by these and similar studies have offered valuable insights into hydrothermal fluid chemistry, each of these techniques has limitations for quantitative, non-destructive analysis of individual fluid inclusions. Recently, synchrotron X-ray fluorescence (SXRF) has been shown to be a promising technique for in situ, non-destructive qualitative to semi-quantitative analysis of individual natural (RANKIN et al., 1992) and synthetic (FRANZ et al., 1988; VANKO et al., 1993) fluid inclusions. A general description of synchrotron radiation applications in the earth sciences is provided by BASSETT and BROWN (1990), and a detailed review of SXRF is provided by RIVERS et al. (1991).

The purpose of this study was to develop and rigorously test the SXRF technique for quantitative analysis of individual fluid inclusions. Previous attempts to use SXRF for fluid inclusion analyses have used theoretical models which assume an ideal analytical geometry to interpret spectra and calculate metal contents. However, these models were not tested by analyzing fluid inclusions of known concentration and non-ideal geometry. In this study synthetic fluid inclusions of known $SrCl_2$ composition were manufactured and analyzed. After determining the geometry of each inclusion analyzed, the calculated Sr concentration was compared to the actual (known) concentration, and those factors which most affect quantitative analysis were identified.

EXPERIMENTAL DESIGN

The intensity of the XRF spectrum for a given element in a natural sample is a function of (i) the analytical volume being excited by the beam, (ii) the concentration of the element in the analytical volume, and (iii) interferences from the host phase or from phases not contained within the analytical volume. In the case of fluid inclusions in quartz, the analytical volume is that volume of fluid in the inclusion through which the beam passes. Similarly, interferences are provided by phases other than the fluid phase contained either in the inclusion or in the quartz host, and by the host quartz itself.

In order to evaluate the relative importance of each of these factors in quantitative analysis of fluid inclusions, aqueous solutions containing known concentrations of various metals were placed into silica-glass capillaries of known wall thickness and inner diameter (permitting accurate determination of analytical volume) and analyzed with SXRF. Results obtained from capillaries were then used as standards against which spectra obtained from inclusions of known geometry and analytical volume, but unknown concentration, could be compared.

Fluid inclusions selected for SXRF analysis were photographed before the analysis so that specific fluid inclusions could be located afterwards, either to conduct duplicate analysis or to measure the inclusion geometry. A modified spindle stage (as described by ANDERSON and BODNAR, 1993) was used to determine the depth (*d*, Fig. 3.1) and thickness of each inclusion selected for analysis. Synchrotron X-ray fluorescence analyses were performed on beam line X26A of the National Synchrotron Light Source, Brookhaven National Laboratory, Upton, New York. At the start of every session the analytical set-up was optimized by maximizing elemental ratios on a standard polished section of anorthite ($CaAl_2Si_2O_8$). The beam focus and position were established using a polished fluorescent material (CsI). The beam size was measured by scanning across a sharp-edged Au grid in the X and Y directions. The beam width is defined, by convention, as equal to the distance between 20% and 80% of the Au peak height. In the X direction (normal to the beam) the beam width is simply that distance, but in the Y direction the beam width is taken as the distance between 20% and 80% of the Au peak height divided by $\sqrt{2}$ because the beam crosses the sample at 45°. For all of the analyses presented here, the beam measured approximately 8 μm by 12 μm.

The doubly polished quartz chip containing pre-selected fluid inclusions was mounted on a pure silica glass disc and placed in a vertical, motorized X-Y-Z stage in the X-ray hutch. An optical microscope with a video camera positioned at 90° to the sample surface allows direct observation of the sample (Fig. 3.1). Samples were excited by a white light (continuum energy spectrum) beam covering the range 3 to 30 keV. X-ray spectra were collected, in air, using a Si(Li) energy dispersive detector positioned at 90° to the beam (Fig. 3.1). One and two dimensional scans were made by mechanically moving the sample stage in the X (horizontal) and/or Y (vertical) directions. The incoming beam penetrates the sample at 45° to the polished surface, and the detector is also positioned at 45° to the sample. Therefore, the path length through quartz is equal

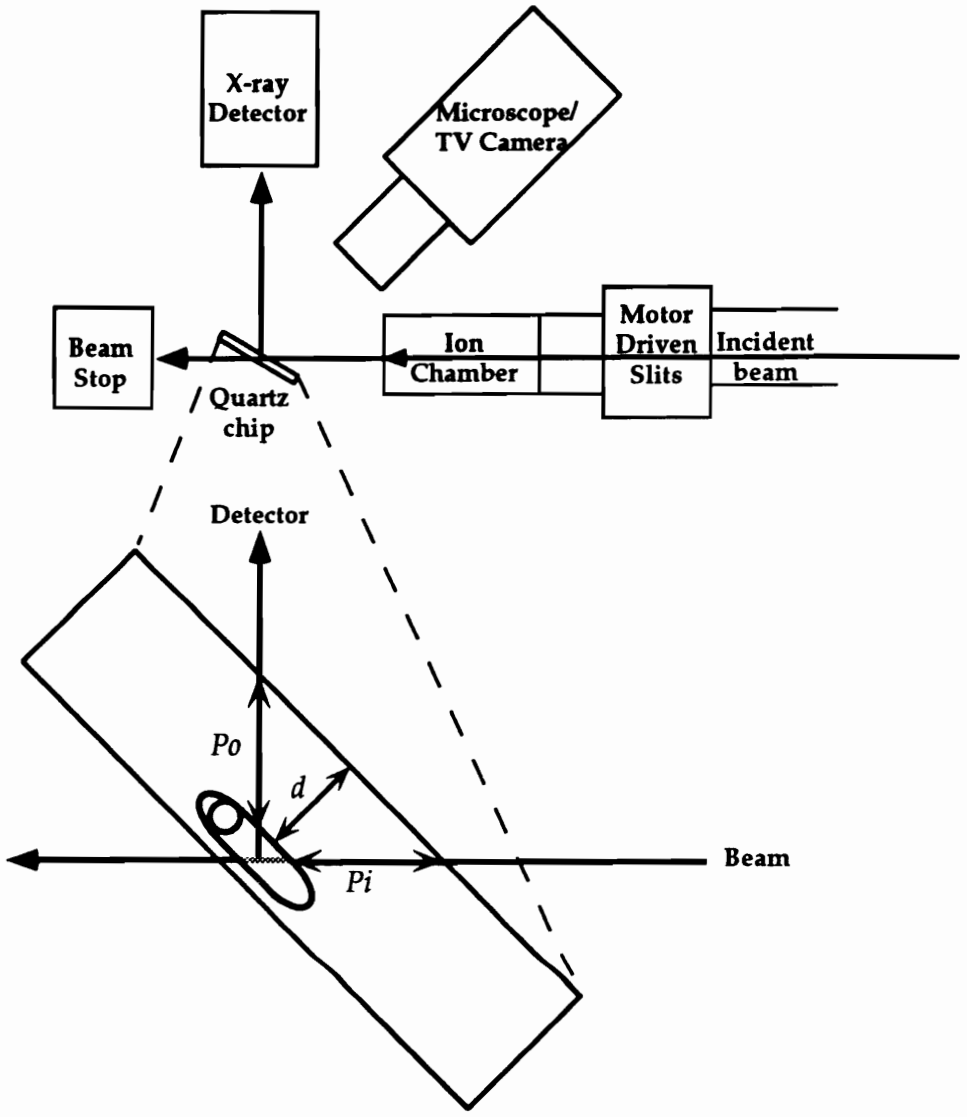

FIG. 3.1. Schematic diagram of the experimental setup at beamline X26A (from Bassett and Brown, 1990), Inset; schematic diagram of an idealized fluid inclusion in a doubly polished quartz chip. Note the pathlength through quartz of the incoming beam (Pi), and the outgoing X-rays (Po), and the inclusion depth (d). The pathlength of the beam within the inclusion is stippled.

for the incoming beam (*Pi*, Fig. 3.1) and the outgoing X-rays (*Po*, Fig. 3.1) generated from the inclusion. From the inclusion depth the path length is easily determined since path length = depth / sin 45°, or depth / 0.707. The path length through the inclusion (stippled beam path, Fig. 3.1) is measured by rotating the sample 45° (on an axis perpendicular to the beam direction) and measuring the thickness of the inclusion at the point where the beam passed through it (Fig. 3.1).

Because light refracts as it enters quartz while the synchrotron X-ray beam does not, the beam location is not always obvious when focusing below the polished surface. Therefore, it is necessary to scan across each inclusion (or set of inclusions) before selecting the spot for analysis. The sample must be carefully examined to insure that there are no other inclusions in the beam path above or below the inclusion of interest. Fig. 3.2B shows a scan across a fluid inclusion (represented by Fig. 3.2A) containing 2,662 ppm Sr. The inclusion of interest was analyzed at the point of maximum intensity to insure that the thickest portion of the inclusion was analyzed. SXRF-EDS spectra were collected (for 60-300 seconds), and elemental peaks were identified at characteristic energies. When a fluid inclusion is viewed from the side (rotated 90°), although its thickness may be variable, its maximum thickness is measured. Therefore, to insure that the beam passed through the measured inclusion thickness, it is important to analyze the inclusion at its thickest point. The point at which the beam pierces the inclusion of interest is marked on a photograph and the inclusion thickness is measured at that point. By multiplying the path-length through the inclusion by the beam dimensions (8 x 12 μm) the excitation volume within that inclusion is determined. A spectrum was also collected from the quartz host next to each inclusion to determine background concentrations of the metal(s) of interest. In synthetic fluid inclusion samples, background elements are essentially nil, but in natural samples the quartz can contribute

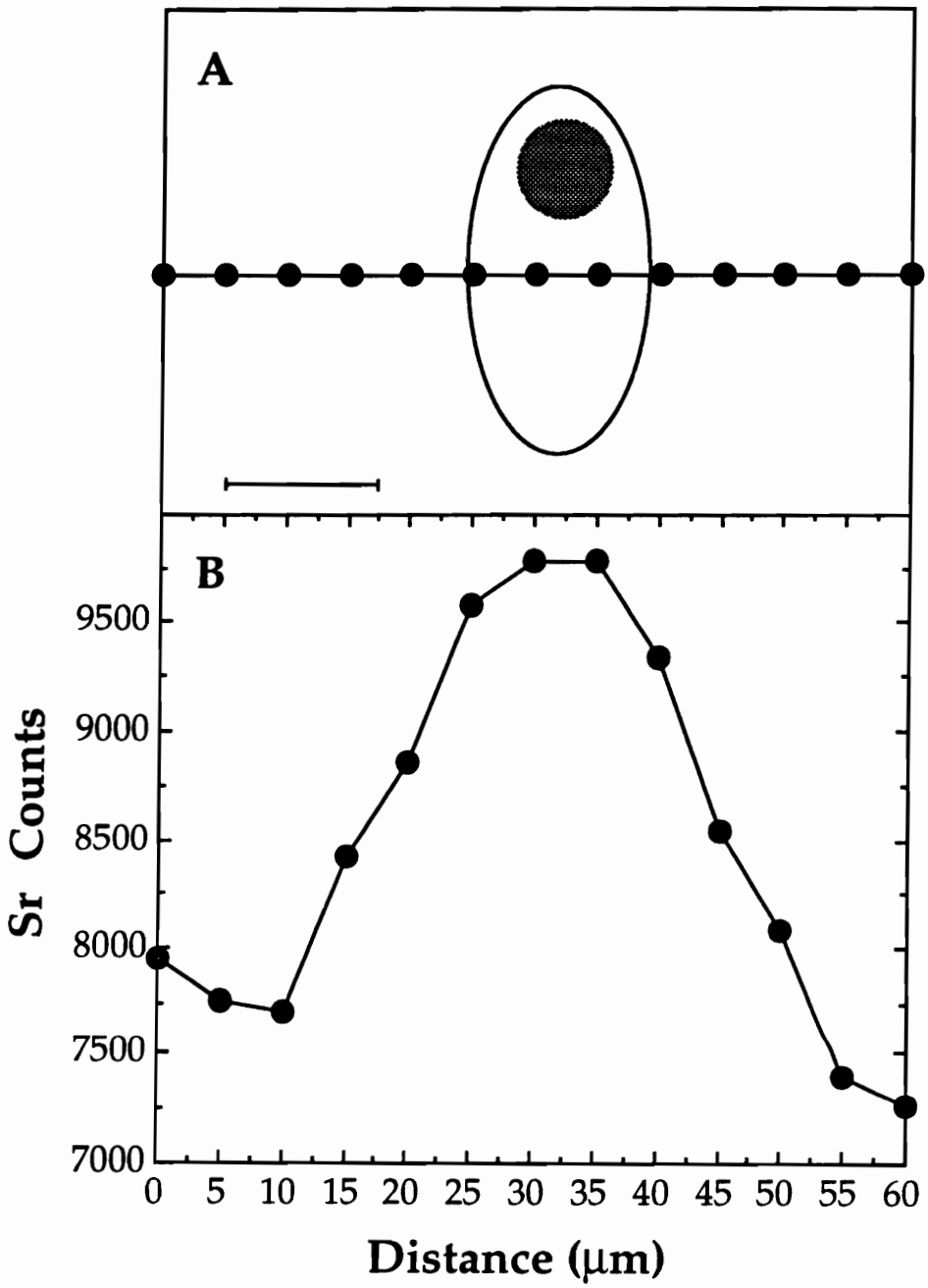

FIG. 3.2. Sr X-ray counts versus distance (B) for a scan across a fluid inclusion containing 2662 +/- 639 ppm Sr (A). The scale bar represents the approximate beam width in the scan direction (12 μm).

significant counts, making it difficult to determine when the beam is on the inclusion, and complicating the quantification process.

Capillaries containing solutions similar to those in the inclusions were analyzed as reference standards, thereby eliminating the need for self absorption (X-rays generated by the inclusion that are of low enough energy to be absorbed by the inclusion fluid) correction. As with electron microprobe analyses, standard measurements collected immediately before and/or after each analysis minimize the uncertainties of the beam current. To insure that all of the capillaries contained the same solution, and to minimize evaporation during analysis, the capillaries were vertically suspended in a large solution reservoir.

After all of the spectra were collected, background subtracted peak areas were obtained via standard peak fitting routines. Peak intensities slowly decrease as the beam energy decreases continuously following initial injection of the synchrotron ring. We attempt to correct for this time-intensity effect by using the ion chamber current (the beam current measured just upsteam of the sample, Fig. 3.1) as a "proportionality factor" to correct and compare spectra taken at different times, i.e. different beam intensities.

Measured intensities were corrected for absorption of the incoming X-ray beam and the outgoing X-rays generated by the sample as they pass through the same thickness of quartz. Correction factors as a function of inclusion depth in quartz, inclusion thickness and concentration were calculated for Sr, Fe, Mn, Zn, Pb and Cu using the Naval Research Lab XRF correction program (NRLXRF) (CRISS, 1977). Although the present study is only concerned with strontium, the correction factors of these other elements were determined for use in a parallel investigation of metals in fluid inclusions from porphyry copper deposits (BODNAR et al., 1993). For thicknesses of 1-30 μm and concentrations from 500-50,000 ppm, the correction factors are essentially independent of concentration and inclusion thickness, depending only on the thickness of quartz

traversed by the incoming beam and the generated X-rays. Correction factors (the ratio of the counts of a specific element produced by the sample assuming there was no quartz filtering the X-rays, divided by the counts for that element after passing through quartz) are presented graphically in Fig. 3.3 as a function of depth in quartz. For any inclusion in quartz whose depth is known, the correction factor is calculated using the equations in Table 3.1.

SXRF analyses of standard solutions in capillaries of known inner and outer diameter were used to demonstrate the correlation between measured counts and excitation volume - the volume of solution encountered by the beam. Figure 3.4 shows the results of horizontal scans across three capillaries of different volume, all containing 1 wt.% Sr. Each scan produces a Gaussian curve with a distinct maximum. This maximum is the point at which the beam is traversing the greatest volume of solution resulting in the maximum number of Sr counts. Spectra were collected from these maximum points for three sets of capillaries (11, 32 and 50 μm i.d.) containing three different solutions and corrected for absorption by the capillary walls. The excitation volume within the capillary plotted against the measured (corrected) Sr counts shows a linear relationship for each composition (Fig. 3.5). The measured counts from any aqueous solution depend (at least in part) upon the volume of that solution encountered by the beam. Therefore, it is clear that to accurately measure metal concentrations in fluid inclusions the excitation volume within each inclusion must be accurately known. The concentration of a metal in an unknown solution is defined by:

$$\frac{(CC^{stand.}) / (IC^{stand.})}{(C^{stand.})(V^{stand.})} = \frac{(CC^{sample}) / (IC^{sample})}{(C^{sample})(V^{sample})} \qquad (3.1)$$

Table 3.1. Correction factors (CF) as a function of depth (d, μm) in quartz for Mn, Fe, Cu, Zn, Pb, and Sr.

Mn	$CF = 0.8584 + 0.0959d + 0.00215d^2 + 0.0007d^3$
Fe	$CF = 0.962 + 0.0507d + 0.00032d^2 + 0.000025d^3$
Cu	$CF = 1.019 + 0.0141d + 0.00033d^2$
Zn	$CF = 1.012 + 0.0127d + 0.000195d^2$
Pb	$CF = 1.0007 + 0.0072d + 0.000037d^2$
Sr	$CF = 0.998 + 0.0037d$

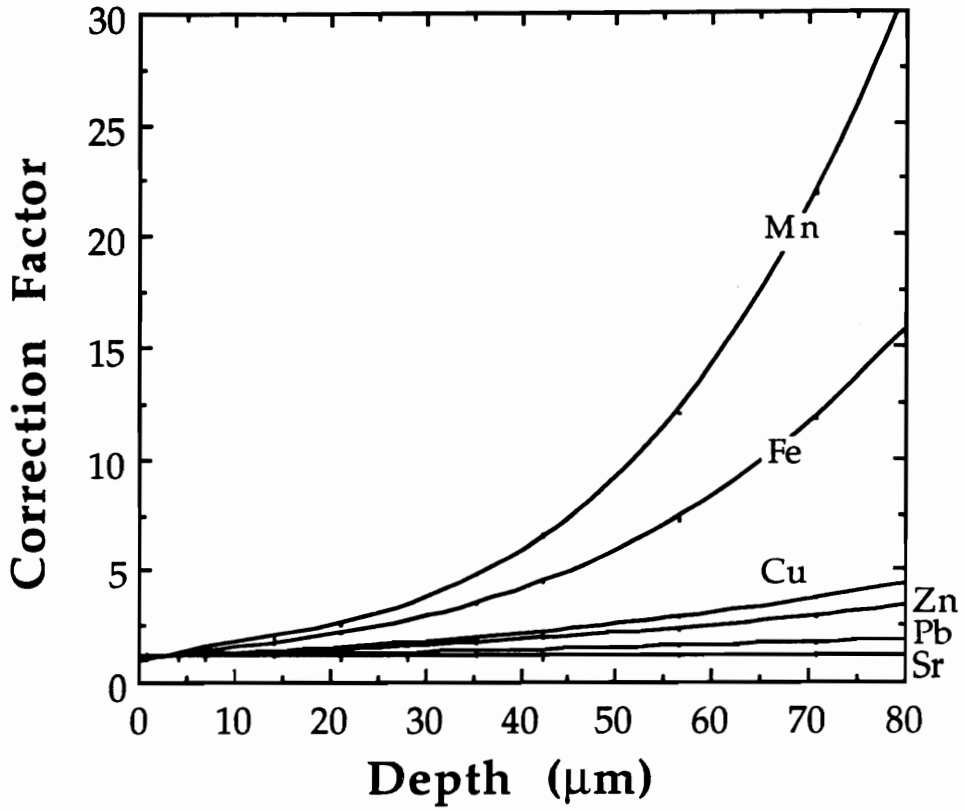

FIG. 3.3. Plot of correction factor versus depth in quartz (μm) for Mn, Fe, Cu, Zn, Pb and Sr.

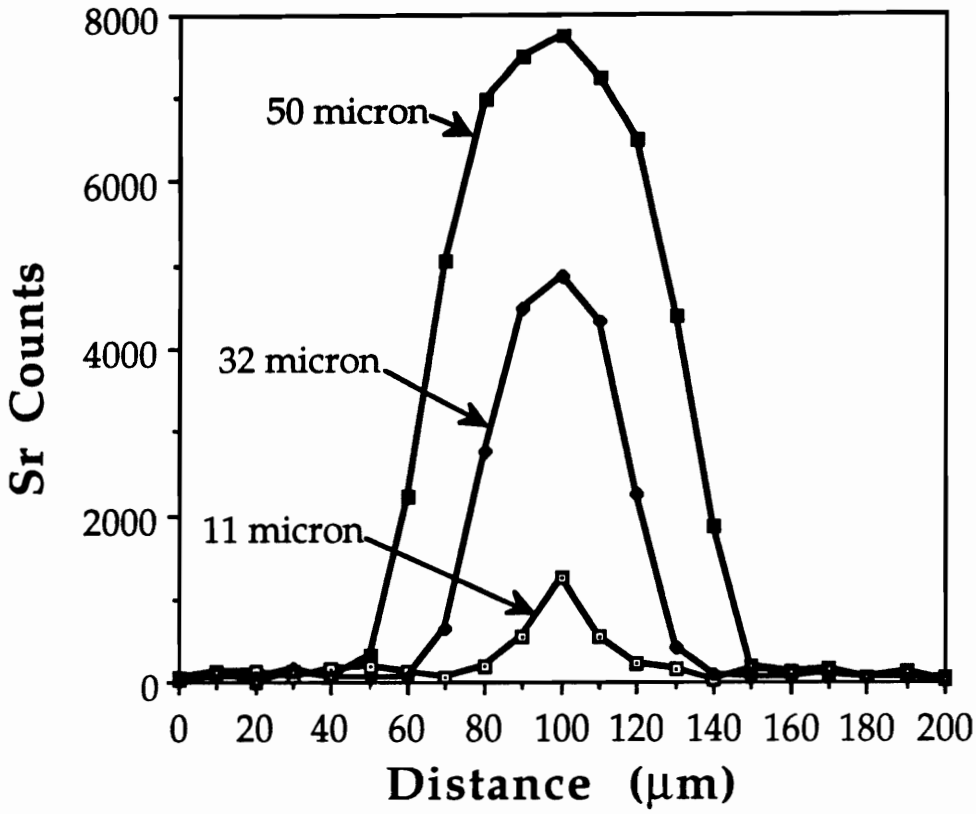

FIG. 3.4. Strontium intensity versus distance (μm) for scans across capillaries of 11, 32 and 50 μm inner diameter containing 1 wt % Sr. Step size equals 10 μm.

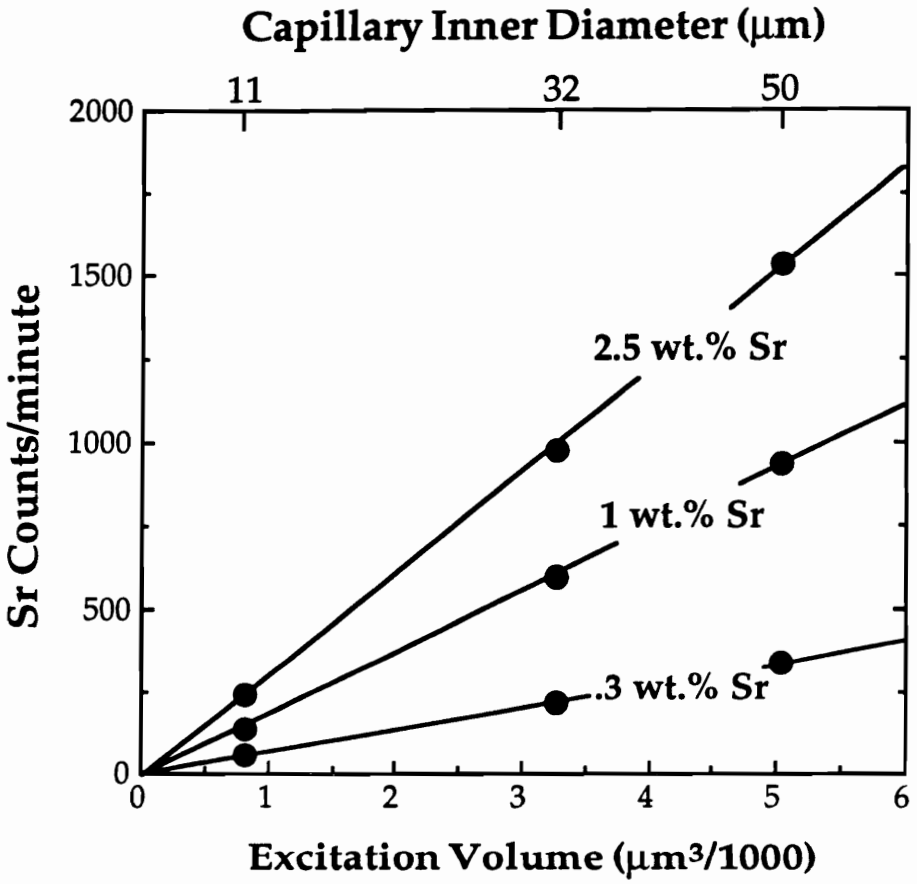

FIG. 3.5. Sr intensities versus excitation volume for capillaries containin 0.3, 1 and 2.5 wt. % Sr. X axis represents capillary inner diameter (upper axis) and calculated excitation volume (lower axis). Each measurement was collected at the position of maximum intensity of a scan across each capillary as shown in Fig. 3.

where CC = corrected counts, IC = ion chamber current, V = volume and **C** = concentration. Superscripts stand. and sample refer to the capillary standard and fluid inclusion, respectively.

Solving for the $\mathbf{C}^{sample}$;

$$\mathbf{C}^{sample} = \frac{(\mathbf{C}^{stand.})(V^{stand.})(IC^{stand.})(CC^{sample})}{(CC^{stand.})(IC^{sample})(V^{sample})} \qquad (3.2)$$

provides the concentration of the element of interest in a specific fluid inclusion.

SYNTHETIC FLUID INCLUSION STANDARDS

To test our SXRF analytical technique, inclusions of known metal content were required. In the early stages of this project, inclusions containing Fe, Cu, Zn and Ag were synthesized because these are the metals that are of most interest in studies of ore-forming systems. SXRF spectra obtained from inclusions from these early experiments lacked peaks for some of the elements in the solutions that were loaded into the Pt capsules. Therefore, it appeared that the inclusions did not trap solutions of the same composition as that loaded into the capsule at the beginning of the run. When the fluids remaining in each capsule after each run were analyzed by AAS, metal concentrations were always lower than the starting composition. Therefore, during the hydrothermal run the composition of the solution changed, and the inclusions formed during the run

trapped solutions of a lower concentration than the starting composition, yet higher than the final composition in the capsule at the end of the run. The discrepancy between the starting composition and that trapped in the inclusions was assumed to be due to one or both of the following processes; 1) alloying of the metal with the Pt capsule (for Sn and Cu, see KEPPLER and WYLLIE, 1991), and 2) metal silicate formation. To minimize this problem, a metal that did not alloy with Pt nor readily form silicates was required to test our technique. It was also desirable to have a metal whose concentration in individual inclusions could be determined by an independent technique for comparison with the SXRF analyses.

To insure that the compositions of synthetic fluid inclusion standards were known, and could be verified by an independent technique, we selected $SrCl_2$ solutions because the freezing-point depression of $SrCl_2$ solutions is known (Weast, 1976), Sr silicates are rarely reported, thereby minimizing the possibility of Sr silicate formation, and the energetic Sr X-rays are not significantly attenuated by quartz (Fig. 3.3), thereby minimizing errors resulting from the necessary corrections involved in SXRF analyses. Strontium chloride solutions of various concentrations were loaded into Pt capsules for fluid inclusion synthesis and the fluid remaining in the capsule after completion of the hydrothermal run was analyzed by atomic absorption. Again, we found that the final Sr concentration was lower than the starting concentration. Final melting temperatures for all inclusions were measured to determine the $SrCl_2$ content of each inclusion before SXRF analyses were attempted. All inclusions in a single sample yielded the same melting and homogenization temperatures thereby ruling out Sr variability within a single sample. By combining the initial and final compositions with the compositions determined by heating/freezing measurements, the composition and uncertainties for each sample were established (Table 3.2). In this manner, seven sets of samples of known Sr composition were available for quantitative SXRF analysis.

Table 3.2. Analytical results obtained from $SrCl_2$-bearing synthetic fluid inclusion standards.

Sample Number	Starting Composition (ppm)	Final Composition (ppm)	Melting Temp (°C)	Melting T Composition (ppm)	Composition (ppm)
92293-V	500	247	0> X>-.1	0 - 1723	374 +/- 126
92293-VI	1000	569	0> X>-.1	0 - 1723	785 +/- 216
22294-I	3000	*	-.1> X>-.2	1723 - 3594	2362 +/- 639
100593-III	5000	3680	-.2> X>-.3	3594 - 5441	4340 +/- 660
92293-VIII	10000	*	-.5> X>-.6	9069 - 10850	9535 +/- 466
22294-III	25000	15100	-.9> X>-1.1	16050 - 19410	17730 +/- 1680
50693-III	35000	22040	-1.3> X>-1.5	22670 - 25850	24260 +/- 1590

* Not enough fluid for reliable measurement

A simple experiment was performed to investigate the mechanism for Sr loss during fluid inclusion synthesis. Two sets of Pt capsules of equal size were loaded with 150 μL of $SrCl_2$ solutions of different compositions (25,000 ppm Sr and 500 ppm Sr). One set contained only those solutions, while the other set contained solution plus 0.08 grams of fine-grained quartz. The capsules were sealed, placed in cold-seal bombs and held at 600°C and 2,000 bars for 24, 120, and 430 hours. Upon quenching, solutions were removed from the capsules and analyzed for Sr by AAS. The results (Fig. 3.6) show no Sr loss in experiments without quartz, but significant Sr loss in the capsules containing quartz. Most of the Sr loss occurred over the first 100 hours with little loss over the subsequent 300 hours (Fig. 3.6). Therefore, we assumed that the mechanism for strontium loss from solution involved interaction of the Sr in solution with quartz, either by the formation Sr ($^{+}/_{-}$ Cl) silicates during the run or by adsorption of Sr^{++} onto quartz surfaces. SEM analyses of the solid material (quartz) removed from the Pt capsules at the completion of the experiments detected no Sr, nor did XRD analyses detect the presence of Sr or Sr-Chloro-silicates. Therefore, we assume that strontium loss from the solutions during the hydrothermal runs was the result of adsorption of Sr onto quartz surfaces. Similar problems with adsorption of highly charged (+2,+3) cations onto quartz during crush-leaching analysis is discussed by BOTTRELL et al. (1988). Although we do not have a clear understanding of the mechanism(s) responsible for strontium loss from solution, the results of the present study are not affected by this problem because we know the Sr concentration within the inclusions from freezing-point depression measurements.

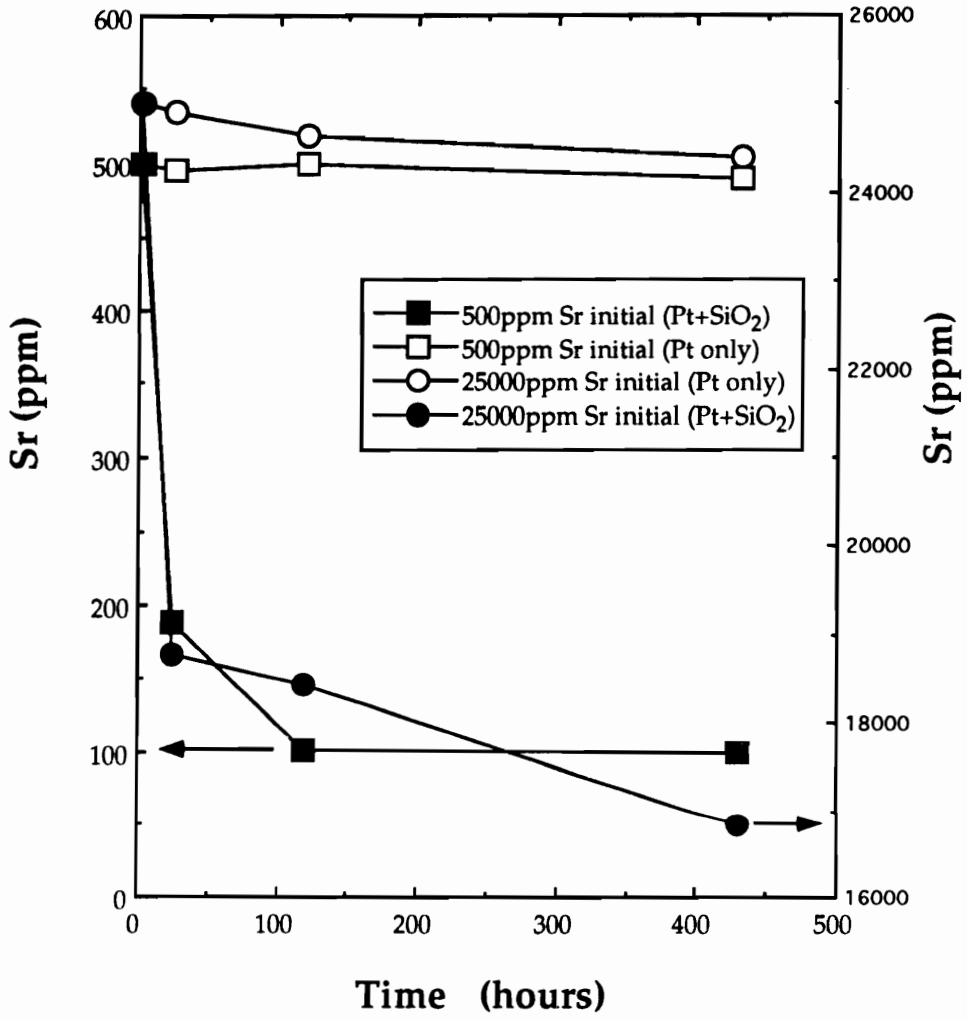

FIG. 3.6. Strontium concentration versus time in $SrCl_2$-H_2O solutions during hydrothermal experiments in sealed platinum capsules. Starting solutions contained 25,000 ppm Sr (square symbols-scale on right axis) and 500 ppm Sr (circular symbols- scale on left axis), solid symbols represent runs containing quartz, open symbols represent solution only.

RESULTS

Using equation (3.2) and results from SXRF spectra and inclusion analytical volume determinations, Sr concentrations were calculated for inclusions in five of the seven samples examined in this study. Fluid inclusions in samples containing 374 (+/- 126) and 785 (+/- 216) ppm Sr did not yield adequate Sr counts for analysis. Scans across these inclusions did not yield Sr counts above background.

The detection limit for metals in fluid inclusions is a function of host sample thickness, inclusion thickness, metal concentration in the inclusion, background metal concentration in the host quartz, and inclusion depth. In 11 μm inner diameter capillaries, the detection limit for Sr is approximately 250 ppm. However, in quartz, the greater total sample thickness, and abundant trace elements present in the host, increase the background tenfold over that from silica glass capillaries. Ideally, quartz chips could be thinned to 30 μm to minimize the background. Unfortunately thin quartz chips are so fragile that they break up when rotated in oil for study of inclusion depths and geometries in the spindle stage. Quartz chips could be thinned after completion of the spindle stage measurements, but thickness measurements must be re-checked after SXRF analyses at the exact position and orientation of the beam in the sample.

Of the samples analyzed for this study, only inclusions containing 2,362 (+/- 639) ppm Sr or more could be quantified. Scans across inclusions containing 2,362 (+/- 639) ppm Sr that were less than 4 μm thick yielded no Sr peak above background. Thus the detection limit for inclusions in the range of 4 to 10 μm thick is some value greater than 1,723 ppm Sr (2,362 - 639 = 1,723). For thicker inclusions, the minimum detection limit is lower than 1,723 ppm, but, greater than 569 ppm (785-216 = 569) because inclusions thicker than 10 μm containing 785 (+/- 216) ppm Sr were below detection. The practical detection limit for Sr-bearing fluid inclusions is somewhere between 1,000 and 1,700

ppm Sr. In this study, the inclusions ranged in thickness from 4 to 18 μm (with the exception of one 30 μm thick inclusion). Detection limits for natural inclusions, that may be much thicker, would be considerably lower, probably as low as several hundred ppm. Strontium can be measured reliably in inclusions as deep as 300 μm (in quartz) but analyses of lighter elements is only possible for much shallower fluid inclusions (see VANKO et al., 1993).

The results of analyses of 33 individual inclusions from samples of five different Sr concentrations are presented in Table 3.3. The known composition range for each sample is listed above the inclusion numbers. Also shown are depth, correction factor (C.F.), corrected counts, inclusion thickness and the calculated Sr concentration (ppm). The mean for each sample and the standard deviation are also listed. Most individual inclusion analyses did not fall within the known composition range for that sample (defined by combining the starting and ending fluid compositions of each run with the compositions obtained from the freezing-point depression measurements of each inclusion in the sample), but the mean value of all of the inclusions in a sample was within the known composition range for three samples containing 2,362 (+/- 639) ppm, 9,535 (+/- 466) ppm and 24,260 (+/- 1590) ppm. The mean of the analyses of the other two samples, containing 4,340 (+/- 660) ppm and 17,730 (+/- 1,680) ppm, fell within one standard deviation of the known composition range.

In Figure 3.7 the known compositions from Table 3.3 are plotted against the measured compositions from Table 3.3, illustrating the large range in individual inclusion results, and the close proximity of the means to the known composition line. Note that the vertical error bars of the uncertainty in the known composition overlap with the horizontal error bars representing one standard deviation of all of the analyses within a single sample. Although the scatter of individual analyses appears to increase with

Table 3.3. Analytical results obtained from 33 individual fluid inclusions of five different $SrCl_2$ concentrations. Fluid inclusion Sr-concentrations (bold case) and sample numbers (italics) are listed for each sample.

Fluid Inclusion#	Depth (μm)	C.F.	Corr. counts	Thick (μm)	Sr ppm	Mean	Stand. Dev.
2362 +/- 639 ppm							
22294-I-							
2	90	1.36	5247.71	9	2457.69	2661.8	280.70
3	100	1.40	6252.79	10	2648.95		
5	160	1.72	3733.80	7	2477.92		
16	60	1.23	6709.14	10	3062.72		
4340 +/- 660 ppm							
100593-III-							
5	60	1.23	3978.87	4	2440.94	2802.9	690.2
6	52	1.19	5022.40	8	3002.57		
7	190	1.90	6183.35	7.5	2023.11		
11	72	1.28	3324.50	8	2189.36		
13	70	1.27	5134.37	7	3491.28		
14	100	1.40	7708.59	10	3670.59		
9535 +/- 466 ppm							
92293-VIII-							
1	5	1.02	3469.88	18	10538.24	9244.5	1313.6
2	37	1.13	1384.60	9	8434.04		
3	30	1.11	1420.76	10	7824.76		
4	27	1.10	1466.22	10	7745.58		
8	85	1.33	1571.73	10	8978.21		
9	95	1.38	2029.80	11	10736.37		
10	59	1.22	2178.65	12	10454.15		
17730 +/- 1680 ppm							
22294-III-							
1-1	5	1.02	10231.02	7	12528.15	14684.3	3469.7
1-2	22	1.08	5898.61	4	12683.54		
1-3	31	1.11	12799.42	9	12221.57		
2-4	120	1.50	20243.05	10	16890.52		
2-5	100	1.40	29806.73	14	17431.52		
2-9	90	1.36	5805.45	4	12130.12		
2-10	55	1.21	10128.23	6	14084.75		
2-12	85	1.33	5810.58	4	12060.57		
2-13	55	1.21	48013.87	18	22128.07		
24,260 +/- 1590 ppm							
50693-III-							
1	21	1.07	67165.15	15	28187.20	22588.9	8785.1
2	16	1.06	15540.22	13	16683.14		
3	46	1.17	42467.59	15	19440.70		
5	25	1.09	46940.99	12	24583.15		
6	70	1.27	11273.04	8	10143.07		
12	5	1.02	180996.95	30	37646.83		
15	27	1.10	10705.69	7	21437.86		

Depth (μm) = distance from upper quartz surface to the top of the fluid inclusion.
C.F. = correction factor (see Fig. 3.3).
Corr. Counts = Sr counts obtained from inclusion after correction (counts * C.F.).
Thickness (μm) = pathlength traversed by the beam through the fluid inclusion.
Sr (ppm) = Sr concentration in inclusion, calculated from SXRF measurements.
Mean = mean of all analyses of a single sample.
Stand. Dev. = The standard deviation of all analyses from a single sample.

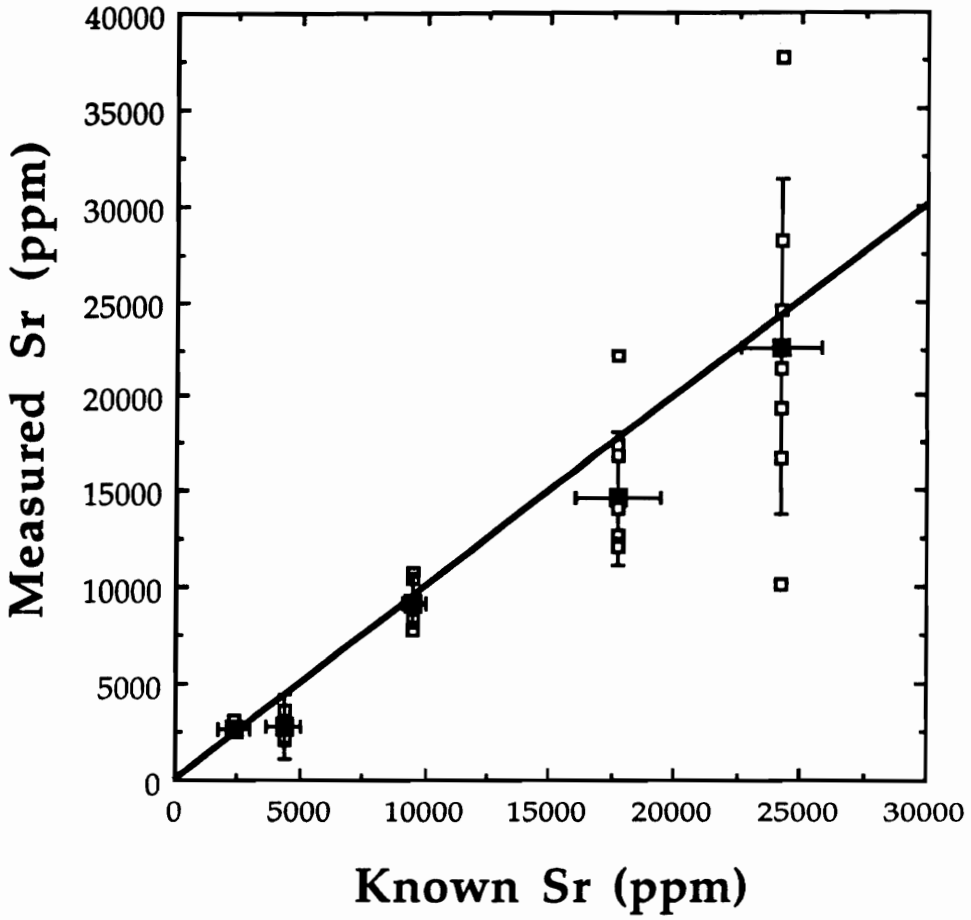

FIG. 3.7. Plot of measured Sr versus known Sr for 33 individual fluid inclusions (open boxes) from samples of 5 different Sr concentrations. Solid squares represent the mean of the measured values for each sample, error bars in the y direction represent the standard deviation for that sample, the error bars in the x direction represent the uncertainty of the known Sr concentration for each sample. The dark black line has a slope of 1 for comparison.

concentration, this is not the case. The magnitude of the variance increases, but, when examined as a percentage of the mean, standard deviations vary from 10-39% of the mean, with no correlation between concentration and the degree of scatter.

DISCUSSION

The goal of this study was to determine the reliability with which quantitative analyses of individual fluid inclusions could be obtained with SXRF, and to identify those analytical factors which most affect quantitative analyses. The major uncertainty in these analyses is the determination of the analytical volume within fluid inclusions. As the capillary analyses showed, an incorrect analytical volume estimate can affect the calculated concentration. For a 2.5 wt.% Sr solution in silica-glass capillaries (Fig. 3.5) an order of magnitude change in the analytical volume (from 500 to 5,000 μm^3) produces an order of magnitude change in the Sr counts (from 1,600 to 16,000 counts). Therefore, an order of magnitude error in the inclusion thickness measurement would produce an order of magnitude increase in the calculated concentration. For inclusions that are highly irregular in 3 dimensions, it is possible that the measured path length through the inclusion and the actual path length could differ by an order of magnitude, thereby producing an order of magnitude error in the calculated concentration.

The path lengths through fluid inclusions that are highly irregular in three dimensions are difficult to determine accurately. Fluid inclusions of constant thickness that lie parallel to the upper polished surface yield the most consistent results because the path length through these inclusions (and therefore analytical volume) is more easily determined accurately. In samples that contain numerous inclusions with different orientations relative to the beam, path lengths through inclusions whose long axes do not lie parallel, or perpendicular to the axis of the spindle stage are some unknown value

greater than the apparent inclusion thickness. Thus, these inclusions yield highly variable compositions because of inaccurate analytical volume determinations.

The large uncertainty associated with individual fluid inclusion analyses and the acuracy of the mean of numerous analyses within a population demands that numerous inclusions within one population be measured and averaged if a representative metal concentration for that population is to be obtained. Furthermore, flat-lying equant, regularly shaped inclusions should be chosen for analysis if quantitative results are sought. As with all fluid inclusion studies, fluid inclusion populations should not be defined by SXRF analyses, but should be pre-determined by paragenetic studies of cross-cutting veins, petrographic observations, heating/ freezing results or any other well established fluid inclusion technique. Unfortunately, the current poor precision of SXRF analyses precludes the use of this analytical technique to monitor variability of metal concentrations in a group of coeval (or nearly coeval) fluid inclusions.

The relatively high detection limits reported herein also preclude meaningful analyses of fluid inclusions from most "non-magmatic" ore deposits. Our preliminary investigations of fluid inclusions from a variety of sediment-hosted ore deposits have, to date, been unsuccessful because these inclusions apparently contain low concentrations of metals. Furthermore, the high levels of trace elements in natural samples and the presence of abundant solid inclusions of variable composition intimately associated with fluid inclusions in these samples makes their quantification difficult at best. In most cases, one should select large inclusions, near the upper polished surface of very clear quartz.

REFERENCES

ANDERSON, A.J., CLARK A.H., MA, Xin-Pei, PALMER, G.R., and MACARTHUR, J.D. (1989) Proton-induced X-ray emission analysis of unopened fluid inclusions. *Econ. Geol.* **84**, 924-939.

ANDERSON, A.J., and BODNAR, R.J. (1993) An adaptation of the spindle stage for geometric analysis of fluid inclusions. *Amer. Mineral.* **78**, 657-664.

BARNES, H.L. (1979) Solubilities of ore minerals. In *Geochemistry of Hydrothermal Ore Deposits* 2nd ed. (ed. H.L. Barnes), 404-460. John Wiley and Sons, New York.

BASSETT, W.A., and BROWN, G.E., Jr (1990) Synchrotron radiation: Applications in the earth sciences. In: *Annual Review of Earth and Planetary Sciences* (ed. G.W. Wetherill) **18**, 387-447.

BODNAR, R.J., MAVROGENES, J.A., ANDERSON, A.J., BAJT, S., RIVERS, M.L., and SUTTON S., (1993) Synchrotron XRF evidence for the sources and distributions of metals in porphyry copper deposits. American Geophysical Union Transactions, *EOS* **74**, 669.

BOTTRELL, S.H., YARDLEY, B. and BUCKLEY, F. (1988) A modified crush-leach method for the analysis of fluid inclusion electrolytes. *Bull. Min.* **111**, 279-290.

CARPENTER, A.B, TROUT, M.L, and PICKETT, E.E. (1974) Preliminary report on the origin and chemical evolution of lead- and zinc-rich oil field brines in central Mississippi. *Econ. Geol.* **69**, 1191-1206.

CRISS, J. (1977) NRLXRF, Naval Research Laboratory Cosmic Program #DOD-00065. Naval Research Laboratory, Washington, D.C.

FRANTZ, J.D., MAO, H.K., ZHANG, Y.-G., WU, Y., THOMPSON, A.C., UNDERWOOD, J.H., GIAUQUE, R.D., JONES, K.W., and RIVERS, M.L. (1988) Analysis of fluid inclusions by X-ray fluorescence using synchrotron radiation. *Chem. Geol.* **69**, 235-244.

HAYNES, F.M., STERNER, S.M., and BODNAR, R.J. (1988) Synthetic fluid inclusions in natural quartz IV. Chemical analyses of fluid inclusions by SEM/EDA: Evaluation of method. *Geochim. Cosmochim Acta* **52**, 969-977.

HEINRICH, C.A, RYAN, C.G., MERNAUGH, T.P., and EADINGTON, P.J. (1992) Segregation of ore metals between magmatic brine and vapor: A fluid inclusion study using PIXE microanalysis. Econ. Geol. **87**, 1566-1583.

HELGESON, H.C. (1992) Effects of complex formation in flowing fluids on the hydrothermal solubilities of minerals as a function of fluid pressure and temperature in the critical and supercritical regions of the system H_2O. *Geochim. Cosmochim. Acta* **56**, 3191-3207.

HORN, E.E., and TRAXEL, K. (1987) Investigations of individual fluid inclusions with the Heidelberg proton microprobe-a non-destructive analytical method. *Chem. Geol.* **61**, 29-35.

KEPPLER, Hans, and WYLLIE, P.J., (1991) Partitioning of Cu, Sn, Mo, W, U and Th between melt and aqueous fluid in the system haplogranite-H_2O-HF. *Contrib. Min. Pet.* **109**, 139-150.

MAASKANT, P. (1986) Electron probe microanalysis of unopened fluid inclusions, a semiquantitative approach. *Neues Jahrb. Mineralogie Monatsch.* **7**, 297-304.

RANKIN, A.H., RAMSEY, M.H., COLES, B., VAN LANGEVELDE, F. and THOMAS, C.R. (1992) The composition of hypersaline, iron-rich granitic fluids based on laser-ICP and synchrotron-XRF microprobe analysis of individual fluid inclusions in topaz, Mole granite, eastern Australia. *Geochim. Cosmochim. Acta* **56**, 67-79.

RIVERS, M.L., SUTTON, S.R., and JONES, K.W. (1991) Synchrotron X-ray fluorescence microscopy. *Synchr. Rad. News* **4**, 23-26.

SHEPHARD, T.J., RANKIN, A.H., and ALDERTON, D.H.M. (1985) *A practical guide to fluid inclusion studies.* Blackie, 239p.

SYMONDS, R.B. (1992) Getting the gold from the gas: How recent advances in volcanic gas research have provided new insights on metal transport in magmatic fluids. *Geol.Surv. Japan* **279**, 170-175.

VANKO, D.A., SUTTON, S.R., RIVERS, M.L., and BODNAR, R.J. (1993) Major-element ratios in synthetic fluid inclusions by synchrotron X-ray fluorescence microprobe. *Chem. Geol.* **109**, 125-134.

WEAST, R.C., ed. (1976) Handbook of Chemisrty and Physics: Cleveland, Ohio, CRC Press.

WEISSBERG, B.G., BROWNE, P.R.L., and SEWARD, T.M. (1979) Ore metals in active geothermal systems. In *Geochemistry of Hydrothermal Ore Deposits* , 2nd ed. (ed. H.L. Barnes), 738-780.

Chapter 4: Vanadium phases in Texaco petroleum-coke gasification slags:

ABSTRACT

The Texaco gasification system developed at the Monte Bello pilot plant efficiently burns petroleum-coke thereby producing syn-gas and electricity. This system produces more electricity than conventional burners, yet the only by-products are pharmaceutical grade sulfur and V-rich slag. Vanadium is known to exist in multiple valence states in compounds which possess a wide range of melting points and physical properties. Consequently, it becomes important to carefully regulate oxygen fugacity throughout the system in order to control vanadium valence state. Vanadium phase equilibria is presently poorly understood, in large part because of the multiple oxidation states of vanadium (-1, 0, +2, +3, +4, and +5) and the difficulty of unequivocally identifying the valence state(s) in many compounds. The operation of these gasifiers at approximately 1400°C is well above the melting point of V_2O_5 but considerably below the melting temperature of VO_2 and V_2O_3. If fO_2 can be regulated to keep the burner within the V_2O_5 field, slag material would more likely remain molten and more easily flow out of the bottom of the burner. In pure V oxides, the oxidation state is readily determined by microprobe analysis, where V_2O_5 (V^{+5}) is 56% V, VO_2 (V^{+4}) is 61.4% V, and V_2O_3 (V^{+3}) is 68% V. However, V valence in multi-element phases (especially phases containing other elements of variable valence) cannot be resolved by microprobe analysis alone. Petroleum-coke gasification slags collected from within the gasifier under different oxidation conditions were studied by electron microprobe analysis (EMPA), X-ray diffraction (XRD), X-ray photoelectron spectroscopy (XPS) and Raman

spectroscopy. Raman spectrometry in conjunction with microprobe analysis was found to resolve the valence of vanadium in the phases of these slags. Raman spectra collected from homogeneous single phase V-oxide standards in vacuum at low temperatures (-180°C) yielded peaks characteristic to each valence state. Gasifier slag samples are, however, much more complicated. Oxidized samples contain: fine grained (Ca, Mg, Fe, V) oxide matrix of variable composition, (Fe, V, Ni) spinel, (Fe, Al, V, Ni, Mg) spinel, V_2O_5 laths, Al-Si glass blebs and Ni sulfides. Reduced samples contain: crystalline Ca-silicate matrix, subhedral to euhedral (V, Fe, Mg, Al) spinel, subhedral VO_2, Fe and Fe-Ni sulfides, Fe-Ni alloys, and complex Ca-oxide matrix. The different spinel assemblages, the characteristic V-oxides and the distinctly different character of the matrices makes the oxidized and reduced slags readily discernible.

INTRODUCTION

Concerns for the depletion of high quality liquid crude oils and the desire of energy companies to increase efficiency in energy production is leading to the consideration of new alternatives. Gasification of coal and petroleum coke is a promising method that can not only burn waste without air pollution, but very efficiently generate gases which may be used in chemical synthesis, electrical generation, or heat production. Texaco has conducted an extensive pilot plant test program at the Monte Bello Research Laboratory to optimize the Texaco Gasification Process using petroleum coke, the residuum solid remaining after refining, as a feed stock. Petroleum coke is burned at approximately 1400° C in a controlled environment to produce "syn-gas", a mixture containing mostly CO and H_2. When used for electrical production, this system is very efficient and produces more electricity than conventional burners, yet the only by-products are pharmaceutical grade sulfur and slag. As the price of fuels and the costs of waste

disposal increase, gasification systems using petroleum coke, coal, sewage sludge and municipal waste will become leading options for power generation.

The geochemically anomalous concentrations of vanadium in petroleum, in general, and in heavy crudes, in particular, lead to the extraordinary enrichment of vanadium in the slags that form as a result of the gasification process. The enrichment of V from petroleum to gasifier slag can be as great as 10,000 times (GROEN, 1991). Interest in the V compounds stems from their highly variable physical characteristics in slags, the potential for recovery, and concerns regarding disposal. This study was undertaken to examine vanadium-rich slags and synthetic analogs in order to identify phases, characterize their behavior, and attempt to predict methods to modify them. Techniques employed included: reflected light microscopy, scanning electron microscopy with energy dispersive spectrometry (SEM-EDS), electron micro-probe analysis (EMPA), X-ray diffraction (XRD), X-ray photoelectron spectroscopy (XPS) and laser Raman spectroscopy. Vanadium phase equilibria is presently poorly understood, in large part because of the multiple oxidation states of vanadium (-1, 0, +2, +3, +4, and +5) and the difficulty of unequivocally identifying the valence state(s) in many compounds.

The slags are generated as a result of the combustion of petroleum coke at temperatures of 1400°C in large cylindrical gasifiers. Reactants are fed into the top of the preheated gasifier where it burns as it passes through the system (Fig. 4.1). Fine particulate matter released during combustion either passes through the system entrained by gases, or precipitates on the walls of the gasifier. That which precipitates either remains stationary (especially if it is crystalline) or flows as a viscous fluid down the sides of the gasifier. Ideally, the slag either breaks loose or flows out of the bottom of the gasifier and drops into the quench tank. If the material that is sliding down the walls of the burner is too viscous, or crystallizes, it will not flow out of the bottom of the burner. This slag build-up retards proper flow through of material, and reduces the efficiency of

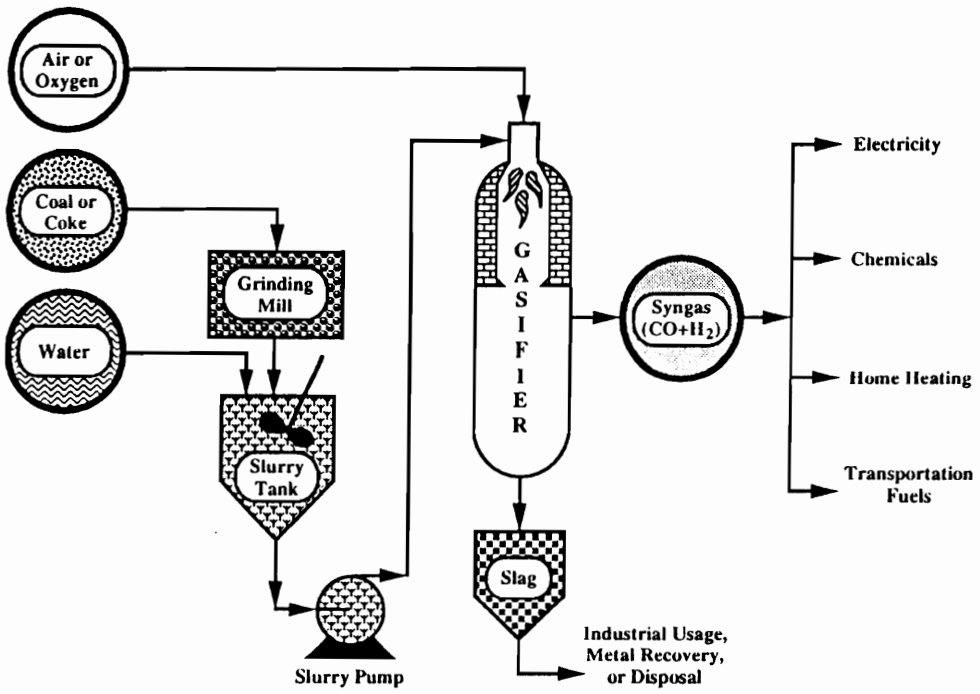

FIG. 4.1. Schematic diagram of the Texaco gasifier system, courtesy of Texaco.

the unit. In early pilot runs, Ca and other additives were mixed with the feed stock to inhibit the formation of highly refractory materials. CRAIG and NAJJAR (1990), CRAIG et al. (1990) and GROEN et al. (1991) have described the occurrences and compositions of many of the phases in these slags.

Another method to promote the proper flow through of slag materials is to regulate the fO_2 of the system, thereby controlling the oxidation state of vanadium. The operation of these gasifiers at approximately 1400°C is well above the melting point of V_2O_5 but considerably below the melting temperature of VO_2 and V_2O_3 (Table 4.1). If fO_2 can be regulated to keep the burner within the V_2O_5 field, slag material would more likely remain molten and more easily flow out of the bottom of the burner.

Table 4.1. Melting point of Vanadium Oxides. (From: Clark, 1973)

Valence	+5	+4	+3	+2
Phase	V_2O_5	VO_2	V_2O_3	VO
Melting Pt.	658°C	1637°C	1967°C	950°C

TECHNIQUES

The main objective of this project has been the detailed characterization of slag samples collected from specific positions within the gasifier system and the effects of oxidation upon them. This characterization includes elemental distribution (phase composition) and vanadium oxidation state. In pure V-oxides, the oxidation state is readily determined by microprobe analysis, where V_2O_5 (V^{+5}) is 56% V, VO_2 (V^{+4}) is 61.4% V, and V_2O_3 (V^{+3}) is 68% V. Vanadium does not appear to occur in a valence state less than V^{+3} in the samples examined in this study. However, there are very few

pure phases in coke gasifier slags, and it is very difficult to determine V valence in multi-element phases. This difficulty, and the importance of transition metals in advanced materials, such as semi-conductors, has led scientists to experiment with such varied techniques as Raman Spectroscopy, Mossbauer analysis, XRF Kα/Kβ ratios, X-ray absorption near edge spectroscopy (XANES), and X-ray photoelectron spectroscopy (XPS) to name only a few, in attempts to determine valence state.

Samples

The following samples from the Texaco Monte Bello experimental gasifier were supplied for study (with Texaco's accompanying sample descriptions):

Set I:
I-1: Coarse Slag DCEP Shutdown
I-2: MRL DCEP Outer Throat Unoxidized 2/13/92
I-3: MRL DCEP Shutdown Oxidized
I-4: MRL DCEP Reduced Slag - Top of Gasifier
I-5: MRL DCEP Unoxidized Inner Throat 2/13/92

Set II:
II-1: Post Deslagging Throat Plug "Stalactite"
II-2: Post Deslagging Throat Plug - Dense Chunk
II-3: Coarse Deslagging Slag after Shutdown
II-4: Coarse Gasification Slag, During Operation
II-5: Post Deslagging Material on Gasifier Wall after Shutdown
II-6: Deslagging Chunk from Quench

Representative portions of each sample were mounted in cold setting epoxy and subsequently polished using conventional methods as described in CRAIG and VAUGHAN (1981). Following polished section preparation, preliminary reflected light microscopic and SEM evaluations of all of the samples were carried out. Based upon the sample information provided by Texaco, and preliminary mineralogical data, samples were grouped into two categories: "oxidized" and "reduced". This distinction is somewhat relative and simply delineates more oxidized mineral assemblages (oxidized)

from those that are less oxidized (reduced). Samples I-1, I-3, II-1, II-5 and II-6 were classified as oxidized, samples I-2, I-4, I-5 and II-4 were classified as reduced. One sample that was considered "most typical" of each group was selected for thorough, detailed investigation, in an attempt to determine how these samples might best be studied. Sample I-3 and I-4 were selected as representatives of the oxidized and reduced slags respectively. The purpose of this report is to review the extensive analyses carried out on samples I-3 and I-4 specifically, and how those results will affect further studies.

Electron Microprobe Analyses

Detailed elemental analyses, and elemental distribution maps were obtained using a fully automated Cameca SX-50 electron microprobe equiped with a Sun 3160 computer and four wave-length dispersive spectrometers. Analyses were performed using a 15 KV excitation voltage and 20 nA sample current.

Laser Raman Spectroscopy

Optical microscopy and electron microprobe analyses of petroleum coke slags characterize the phases present, and the elemental composition of the phases. However, the exact valence states of V within those phases is not easily determined. Laser Raman spectroscopy can potentially identify the valence states of vanadium within complex phases. Initially, Raman spectra were produced with a 100 mW Argon laser and collected with a PMT detector on a Jobin Yvon U1000 instrument. Extensive experiments showed that the different V oxides yield characteristic spectra in evacuated ampoules. Unfortunately, when spectra are collected from polished slag samples in air, the interaction of the laser beam with the sample oxidizes all V oxides to V^{+5}. This

alteration is known to occur because standard V_2O_3, analyzed in air, forms an altered crater where the analysis was made, and a V_2O_5 spectra is always collected. However, Raman spectra collected from samples in an evacuated Joule-Thompson stage at very low temperatures (-180°C) using a Dilor XY Raman microprobe with very low laser power (5mW) and a CCD detector array, reveal no alteration. Standards analyzed in this manner yield peaks charateristic of each valence state (Fig. 4.2). Raman spectra do not equivocally fingerprint a given valence, but, each V-oxide standard produced characteristic peak(s). V_2O_5 yields a recognizable doublet at 141-147 cm^{-1}, V_2O_4 yields a weak peak at 267 cm^{-1} and V_2O_3 produces three distinctive peaks at 156, 260 and 510 wavenumbers (Fig. 4.2). These same characteristic peaks were acquired from polished samples, loose grain mounts at a variety of orientations, and from samples consisting of V oxides mixed with a variety of other compounds. Spectra collected from a mixture of two standards contained the characteristic peak(s) of each valence state present in the sample in proportions approximately relative to the abundance of the phase. Raman analyses are very sensitive to the presence or absence of V_2O_3, but less sensitive to the higher oxidation states, and exact proportions of different valences cannot be derived from the spectra. In complex samples where microprobe analyses do not resolve the valence state, Raman spectroscopy, although inconclusive, helps determine which valences are present.

X-ray Photoelectron Spectroscopy (XPS)

XPS is one of the most promising techniques for transition metal valence determinations. Using V peak positions and widths, standard V oxides of different valence states are readily distinguished. However, mixed V valence states have proven more difficult to identify. XPS analyses of these slag samples confirm that the oxidized

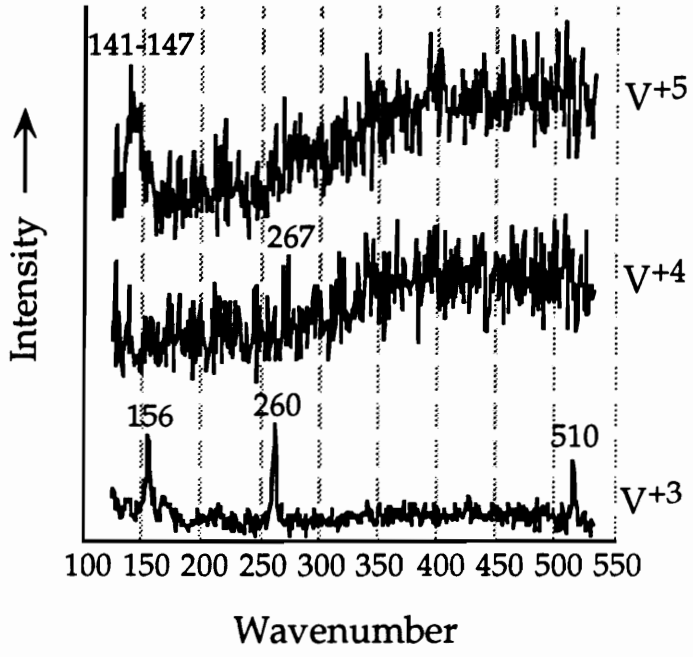

FIG. 4.2 Characteristic Raman spectra of vanadium oxide standards.

samples are dominated by V^{+5} whereas the reduced samples have a much greater V^{+4} component. However, the large beam size of XPS (XPS samples an area 200 x 200 μm) makes analysis of small grains, as in these samples, very difficult.

X-Ray Diffraction

X-ray diffraction patterns from slag material are of very low intensity, with very high background, apparently due to the poorly crystallized nature of this material. Both slags yield characteristic spinel peaks, but the quantities of sulfide and VO_2 in the reduced slag, and V_2O_5 and sulfide in the oxidized slag are too low to produce identifiable peaks. The fine grained, glassy nature of this slag material most likely precludes the use of XRD to identify phases in this material.

Spinel Composition Calculations

As suggested by GROEN et al. (1991), spinel compositions are somewhat problematic, because the variable valence state of Fe and V makes their exact compositions difficult to resolve. If only one element exists in various oxidation states, spinel compositions can be directly determined, but two variable elements requires that certain assumptions and restrictions be applied to the calculations. Laser Raman analyses were used to determine which V valence was dominant in each spinel. In spinels whose Raman analyses suggested that V^{+4} was the dominant V species (i.e. not predominately V^{+3}), all V^{+4} was assigned to the X site and (Mg, Ni) and Fe^{2+} were assigned to the Y site of an inverse "V-ulvospinel" formula of $X^{+4}Y_2^{+2}O_4$. In spinels that appeared to contain V^{+4} and significant amounts of V^{+3}; Mg, Ni and Fe^{+2} were assigned to the X site, and Mg, Fe^{+3} and V^{+3} were assigned to the Y site of a spinel of formula $X^{+2}Y_2^{+3}O_4$.

RESULTS

Oxidized samples contain: fine grained (Ca, Mg, Fe, V) oxide matrix of variable composition, (Fe, V, Ni) spinel, (Fe, Al, V, Ni, Mg) spinel, V_2O_5 laths, Al-Si glass blebs and Ni sulfides (Table 4.2). The reduced samples contain: crystalline Ca-silicate matrix, subhedral to euhedral (Mg, Al, Fe, V) spinel, a subhedral VO_2, Fe and Fe-Ni sulfides, Fe-Ni alloys, and complex Ca-oxide matrix (Table 4.2).

Because of the homogeneous nature of the oxidized slag samples, the phases present and their variation can be well described by examining one selected region of sample I-3. The heterogeneous nature of the reduced slag requires that three regions of sample I-4 be presented to adequately describe the variation of the entire sample.

Table 4.2. Phases and their abundances in oxidized and reduced slag. M = Major (>20), m = minor (5-20%), t = trace (<5%) and - not present.

Phase	Oxidized	Reduced
Fe-V-Ni spinel	M	-
Fe-Al-V-Ni-Mg spinel	M	-
V-Fe-Mg-Al spinel	-	M
V_2O_5	m	-
VO_2	-	M
Ca-Silicate	-	M
Al-Si glass	m	-
NiS	t	-
FeS	-	t
(Fe, Ni)S	-	m
Ni_2Fe	-	m

Oxidized Slag

Oxidized sample I-3 (Fig. 4.3) consists of 5-80 μm phases in a very fine grained groundmass. Two distinct spinels [(i) Fe-Al-V-Ni-Mg bearing; (ii) Fe-V-Ni bearing], and V_2O_5 laths are interpreted as primary phases that grew under the conditions within the gasifier well before quenching. Ni-sulfide and Al-silicate spherules appear to have been immiscible molten droplets within the groundmass and solidified rapidly upon quenching.

Sample I-3 is approximately 20% Fe-Al-V-Ni-Mg oxide spinel which occurs as subhedral, 15-30 μm grains and as larger euhedral hopper crystals up to 80 μm across (Fig. 4.3). The composition and representative variation of this phase is presented in Table 4.3. Raman spectra of these spinels (Fig. 4.5) show the characteristic peaks of V^{+3} and V^{+4} , but compositions work out best with V as V^{+4} , and all Fe as Fe^{+3}. Their compositions differ significantly from other spinels present within these slags in that they contain much higher Mg, Ni and Al. These spinels plot in the higher Al field of Figure 4.4A, and to the Mg, Ni side of Figure 4.4A. Skeletal, hopper crystals appear to be of cubic rather than the more typical octahedral morphology (Fig 4.6). These grains are easily distinguished from the Fe-V-Ni spinel by its lower reflectance, cubic habit, and isotropic character.

Irregular, anhedral Fe-Ni-V oxide spinel grains (25-40 μm across) make up approximately 30% of sample I-3 (Fig. 4.3). This phase shows weak anisotropism in reflected light, and is generally anhedral. Although this phase appears octahedral in polished section (see inset in Fig. 4.3), its structure is most likely slightly distorted, thus the weak anisotropism. Its highly variable Fe content (Fig. 4.7) and low Ni, Mg and Al content (Table 4.3), place its composition toward the Fe_2O_3 end of Figure 4.4A and the

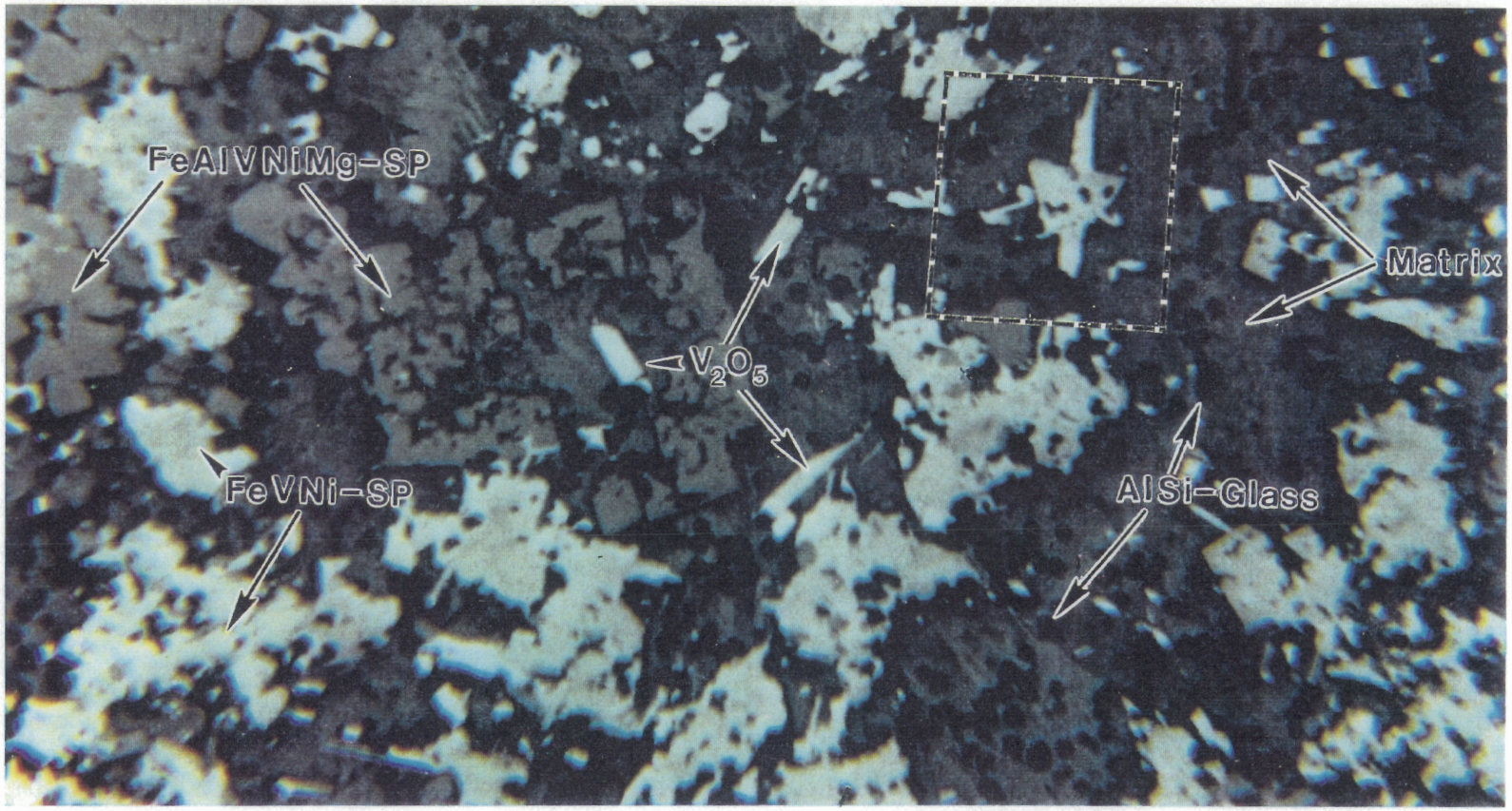

FIG. 4.3. Reflected light photomicrograph of a typical oxidized slag (sample I-3) assemblage (field of view = 250 μm). Outlined area shown in Fig. 4.7.

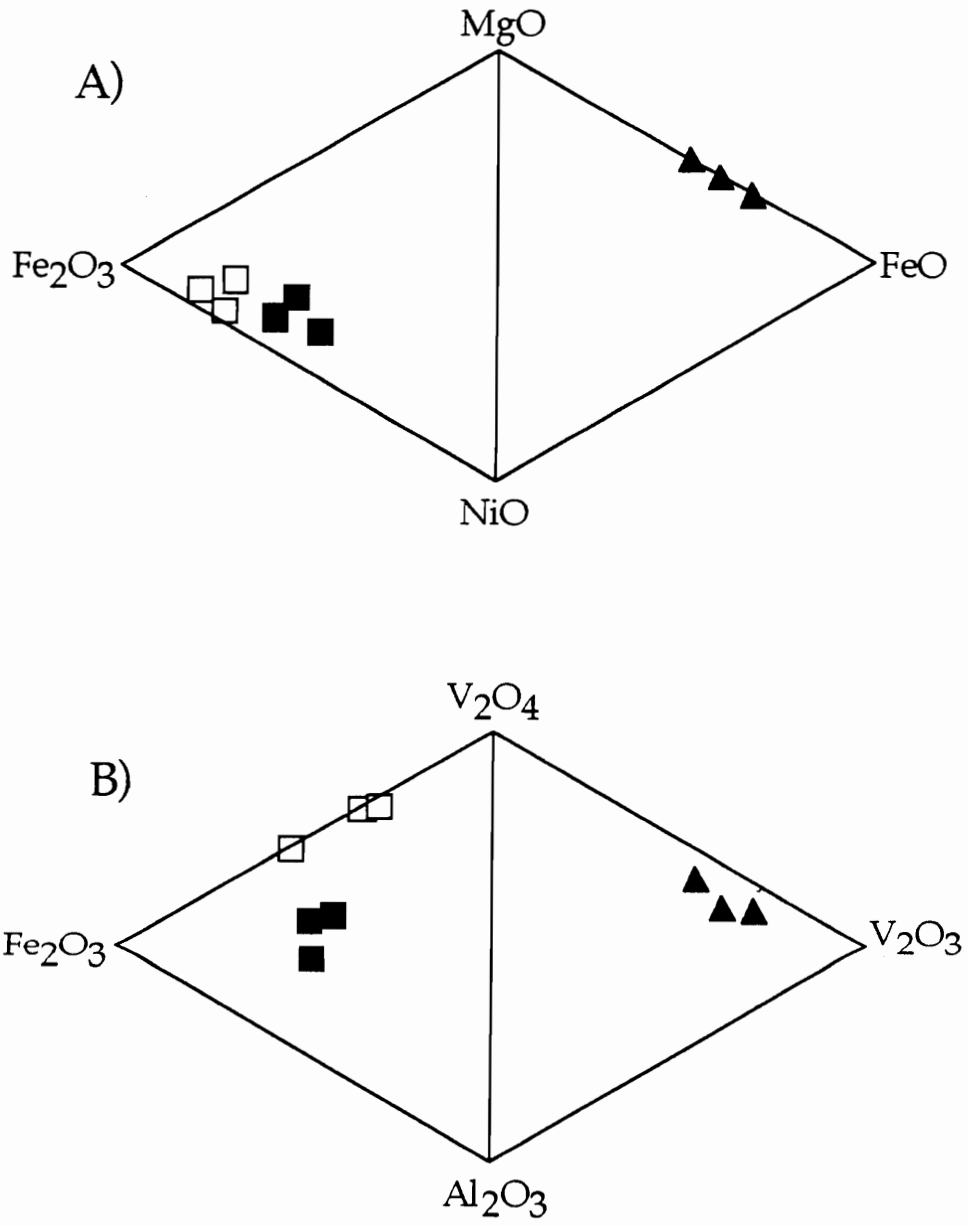

FIG. 4.4. Variation diagram of spinel compositions from oxidized slag (squares) vs. reduced slag (triangles). Filled squares represent Fe-Al-V-Ni-Mg spinels, and open squares represent Fe-V-Ni spinels.

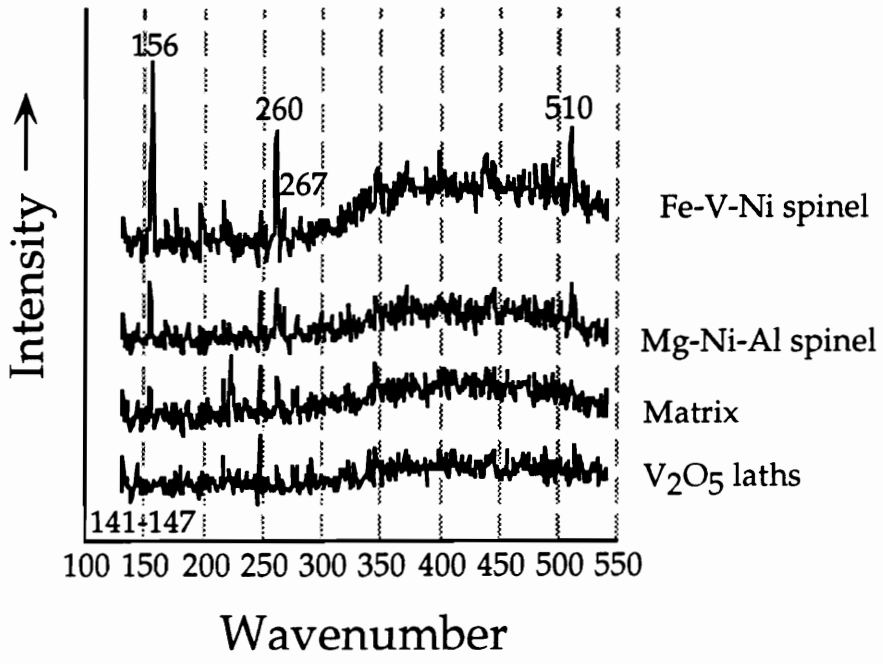

FIG. 4.5. Raman spectra of vanadium-bearing phases in oxidized slag samples.

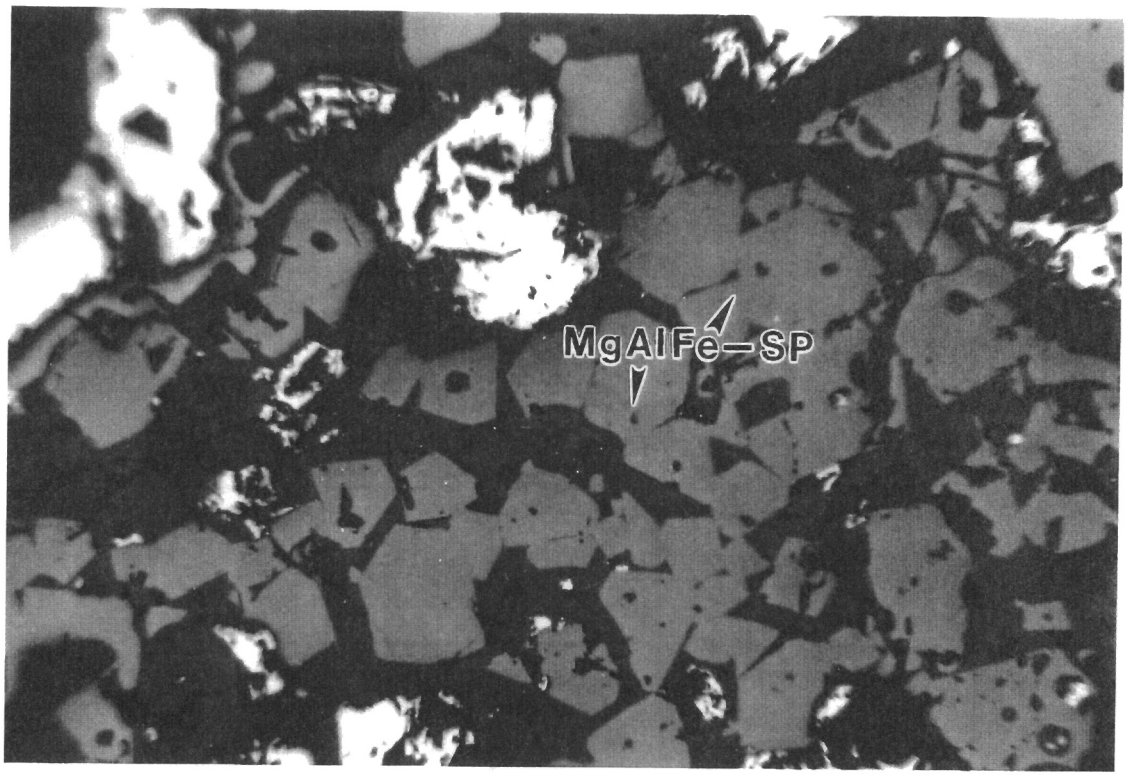

FIG. 4.6. Reflected light photomicrograph showing typical octahedral morphology of reduced slag spinels. Field of view = 200 μm.

low Al side of Figure 4.4B. This spinel is similar to those seen in the reduced slag, except that the spinels in the reduced slag contain reduced V and Fe, and lack Ni.

Table 4.3. Compositional range of Fe-Al-V-Ni-Mg (#1-3) and Fe-V-Ni (#4-6) spinel in oxidized slag.

	Elemental Weight Percent						Oxide Weight Percent					
#	Mg	Al	Fe	V	Ni	Σ	MgO	Al_2O_3	Fe_2O_3	V_2O_4	NiO	Σ
1	4.6	11.3	25.5	9.7	15.4	66.5	7.7	21.3	36.5	15.8	19.6	100.9
2	2.9	7.8	21.4	14.9	17.1	64.1	4.8	14.6	30.6	24.3	21.7	96.0
3	2.9	7.5	26.4	14.0	15.0	63.8	4.8	14.2	37.8	22.8	19.0	98.8
4	1.3	0.0	34.0	24.4	6.6	66	2.2	0.0	48.6	39.8	8.4	99.0
5	0.8	0.0	22.6	34.4	8.3	63	1.3	0.0	32.3	56.1	10.5	100.2
6	0.8	0.8	19.4	35.2	8.3	63	1.3	1.5	27.7	57.4	10.5	98.4

Elemental mapping of the fine grained groundmass material that comprises approximately 1/3 of sample I3 shows it to have a rhythmically banded structure (Fig. 4.7) of unknown origin. This non-stoichiometric material appears to have formed upon quenching. Raman analyses indicate that the V in this material to be V_2O_5 (Fig. 4.5) in that there are no characteristic peaks of the more reduced species. This valence is certainly not due to the run conditions, but rather, apparently reflects quench conditions. The composition of this material is not highly variable (Table 4.4), but microprobe analyses are consistently below 100% suggesting that C may be present in this material.

Table 4.4. Compositional variation of the I-3 matrix in oxidized slag. Since no other elements were detected, it is believed that the low oxide sums reflect either water, carbon or hydrocarbon compounds within the material.

Elemental Weight Percent								Oxide Weight Percent			
Mg	Al	Si	Ca	Fe	V	Ni	Σ	CaO	Fe_2O_3	V_2O_5	Σ
0.1	0.7	0.7	9.3	5.1	33.3	1.0	50.2	13.0	7.3	59.3	79.7
0.1	0.3	0.3	12.6	4.0	32.7	1.3	51.3	17.6	5.7	58.2	81.5
0.1	0.1	0.1	18.5	2.4	34.3	0.4	56.0	25.9	3.4	61.1	90.4

V_2O_5 laths make up approximately 8% of sample I-3. These laths, which are typically in contact with spinel (Fig. 4.3) contain minor Fe and Mg (Table 4.5). The bladed habit of V_2O_5 was confirmed by heating pure V_2O_5 to 750°C and rapidly quenching it in the laboratory, this produced beautiful radiating laths of very similar character. Raman spectra of this bladed phase confirms the presence of V^{+5} (Fig. 4.5), and hence that the material remained V_2O_5 after quenching. Because this phase is present in all of the oxidized samples, and always displays bladed morphology, its presence is one of the defining features of oxidized samples.

Table 4.5. Compositional variation of the V_2O_5 laths in oxidized slag (wt. %)

Elemental Weight Percent					Oxide Weight Percent				
Mg	Ca	Fe	V	Σ	MgO	CaO	Fe_2O_3	V_2O_5	Σ
0.1	0.4	2.2	55.0	57.7	0.2	0.6	3.13	97.8	101.7
0.4	0.3	3.1	53.3	57.0	0.6	0.4	4.39	94.9	100.2
0.1	0.4	2.1	55.8	58.4	0.2	0.6	3.02	99.3	103.0
0.1	0.8	2.2	53.9	57.1	0.3	1.1	3.19	95.9	100.4

Al-Si glass spherules are present in all of the oxidized samples (approximately 5 μm in diameter; Fig. 4.3) and show up clearly in the V and Ca (D and E) maps of Figure 4.7. Its presence within the matrix only, and its perfect spherical morphology lead to the

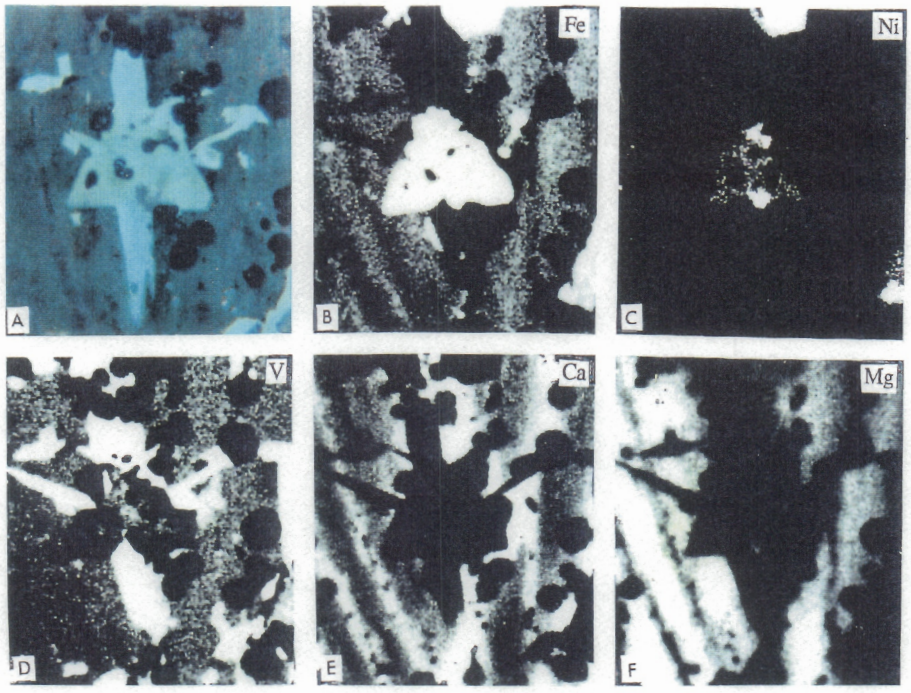

FIG. 4.7. Elemental X-ray maps of the oxidized slag region outlined in Fig. 4.3: A) reflected light photomicrograph, B) Fe distribution, C) Ni distribution, D) V distribution, E) Ca distribution, F) Mg distribution. Field of View = 60 μm.

conclusion that these glass droplets represent an immiscible silicate melt. This glass, which contains minor V, Mg, and Ca, and trace Na, Fe, K and Ni (Table 4.6) comprises approximately 8% of sample I-3.

Table 4.6. Compositional variation of glass spherules in oxidized slag.

Elemental Weight Percent									
Na	Mg	Al	Si	K	Ca	Fe	V	Ni	Σ
1.2	3.6	34.1	34.1	0.2	2.7	0.6	5.0	0.2	81.4
1.0	4.0	30.2	30.2	0.2	1.6	2.6	6.1	0.5	76.1

Very rare, but relatively large (up to 50 μm in diameter) blebs of NiS are present in all of the oxidized samples. The nickel sulfides in the oxidized samples contain little or no iron (Table 4.7) ; in contrast, the sulfides in the reduced samples contain more iron than nickel (Fig. 4.13).

Table 4.7. Compositional variation of Fe, Ni and Fe-Ni sulfides in slags (wt. %)

	Fe	Ni	S	V	Σ
Oxidized:	0.20	62.3	36.8	0.2	99.5
	0.80	63.5	34.8	0.6	99.7
	0.12	64.2	35.1	0.8	100.2
Reduced	62.4	1.6	33.9	0.2	98.1
	62.7	1.4	34.3	0.5	98.9
	49.0	16.7	32.5	0.4	98.6
	41.2	25.6	31.3	0.2	98.3
	40.2	27.1	30.5	0.6	98.4

Figure 4.7 is an elemental map of the 60 μm wide outlined area of the oxidized sample shown in Figure 4.3. Note the high concentration of V in the V_2O_5 laths (Fig

4.7D) and the high concentration of Fe, Ni, and to a lesser extent V in the triangular spinel in the center of the field, also note the banded nature of the Ca, Mg and Fe variation in the matrix (Fig. 4.7B, E, and F). The black spherical areas represent the Al-Si glass blebs. Note also the complete lack of Mg in this Fe-V-Ni spinel (Fig. 4.7F) apparently due to the extreme partitioning of Mg and Ni into the other, more oxidized spinel.

Reduced Slag

Reduced slags are typified by sample I-4 which consists of oxide spinels and VO_2 in a matrix of predominately Ca-oxides. Subhedral to euhedral V-Fe-Mg-Al oxide spinels, commonly in skeletal, and equant euhedral crystals up to 80 μm across (Fig. 4.8) of consistent composition (Table 4.8) make up about 25% of sample I-4. This spinel is composed of $Fe(Fe^{+2})$, V (V^{+3}), Mg and minor Al, but unlike the spinels of the reduced sample it contains no Ni (Fig. 4.4). Its low reflectance, subhedral to euhedral morphology, and isotropic nature make it easily recognizable in reflected light. Reduced slags, such as sample I-4 contain only one spinel type, in contrast to the oxidized samples, which host two distinct spinel types.

Table 4.8. Compositional variation of Spinel in reduced slag.

Elemental Weight Percent					Oxide Weight Percent					
Mg	Al	Fe	V	Σ	MgO	Al_2O_3	FeO	V_2O_3	V_2O_4	Σ
7.4	3.3	10.4	45.5	66.1	12.4	6.2	13.7	50.2	18.5	101.0
6.7	3.5	11.5	44.4	65.3	11.2	6.6	15.2	45.7	21.7	100.4
5.6	3.1	12.8	43.7	61.7	9.4	5.8	16.9	38.5	28.5	99.1

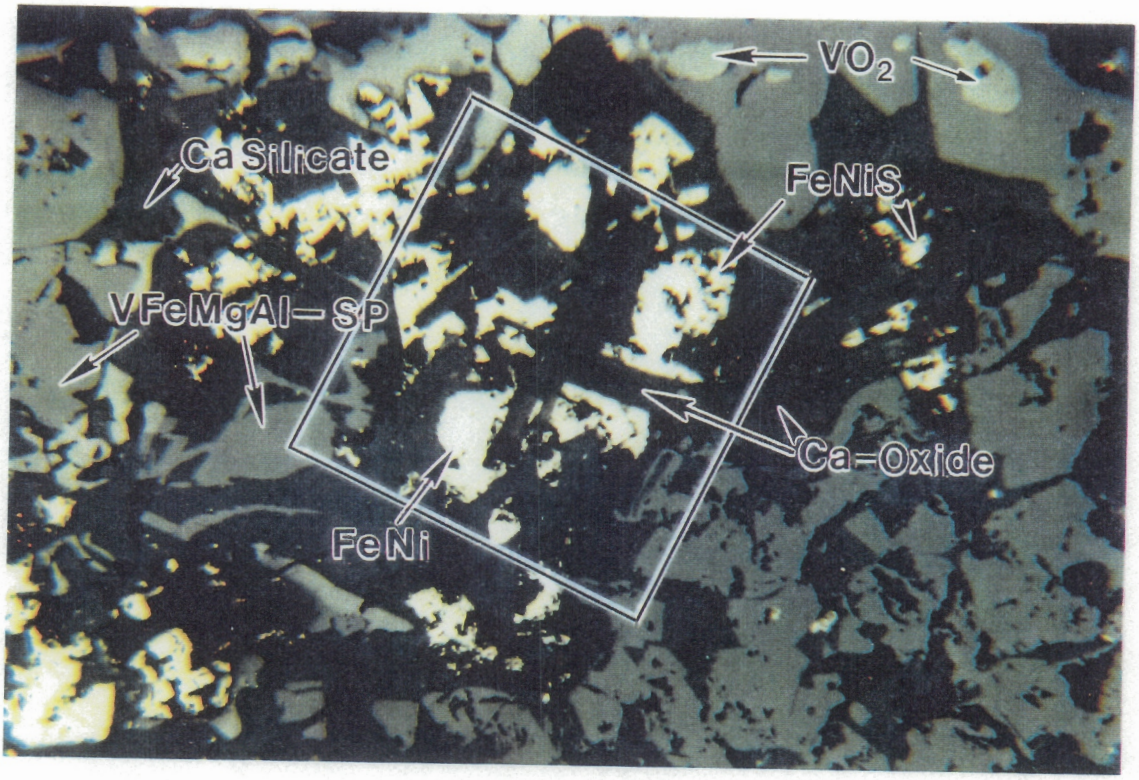

FIG. 4.8. Reflected light photomicrograph of a typical reduced slag assemblage (sample I-4). SP = Spinel. Outlined region shown in Fig. 4.9. Field of view = 350 μm.

VO_2 as rounded subhedral 20-40 μm grains comprises 20% of the sample. This phase is considerably brighter than the spinel phase in reflected light (Fig. 4.8), never displays crystal faces, and is consistently spherical (Fig. 4.9C). This phase looks exactly the same as spinel in BSE due to their coincidentally equivalent atomic weights. Raman spectra show that this predominately VO_2 phase also contains V_2O_3 (Fig. 4.10) as well as small amounts of Mg, Al and Fe (Table 4.9).

Table 4.9. Compositional variation of VO_2 in reduced slag.

Elemental Weight Percent					Oxide Weight Percent					
Mg	Al	Fe	V	Σ	MgO	Al_2O_3	FeO	V_2O_3	VO_2	Σoxides
0.7	0.9	1.6	61.2	64.3	1.1	1.7	2.0	29.4	67.2	100.4
0.6	0.9	1.7	60.2	63.4	1.0	1.7	2.2	23.3	72.0	100.2

The matrix material consists primarily of two distinct phases containing Ca, Si, V, Mg, Al and Fe, and oxygen. On the basis of the dominant elements of each phase, these phases are referred to as Ca-silicate (Table 4.10) and Ca-oxide (Table 4.11), although these terms refer only to the principal elements. These two phases are distinct in reflected light because of the higher reflectance of the Ca-silicate phase (Fig. 4.8). The low reflectance matrix (Ca-Oxide) plots towards the CaO corner of Figure 4.11, and as shown in Figure 4.9F this phase is the most Ca-rich phase in the slag. The Ca-silicate phase is very rich in SiO_2 (Fig. 4.11, and Fig. 4.9D). Raman analyses clearly show that V^{+3} is present in the matrix material (Fig. 4.10). Note the greater abundance of V_2O_3 in the Ca-silicate phase (Fig. 4.9, and Fig. 4.7C). The Ca-oxide phase contains small high phosphorous regions possibly of apatite composition (Fig. 4.9B). As with the reduced slag matrix, microprobe analyses do not total 100%, possibly due to the presence of C.

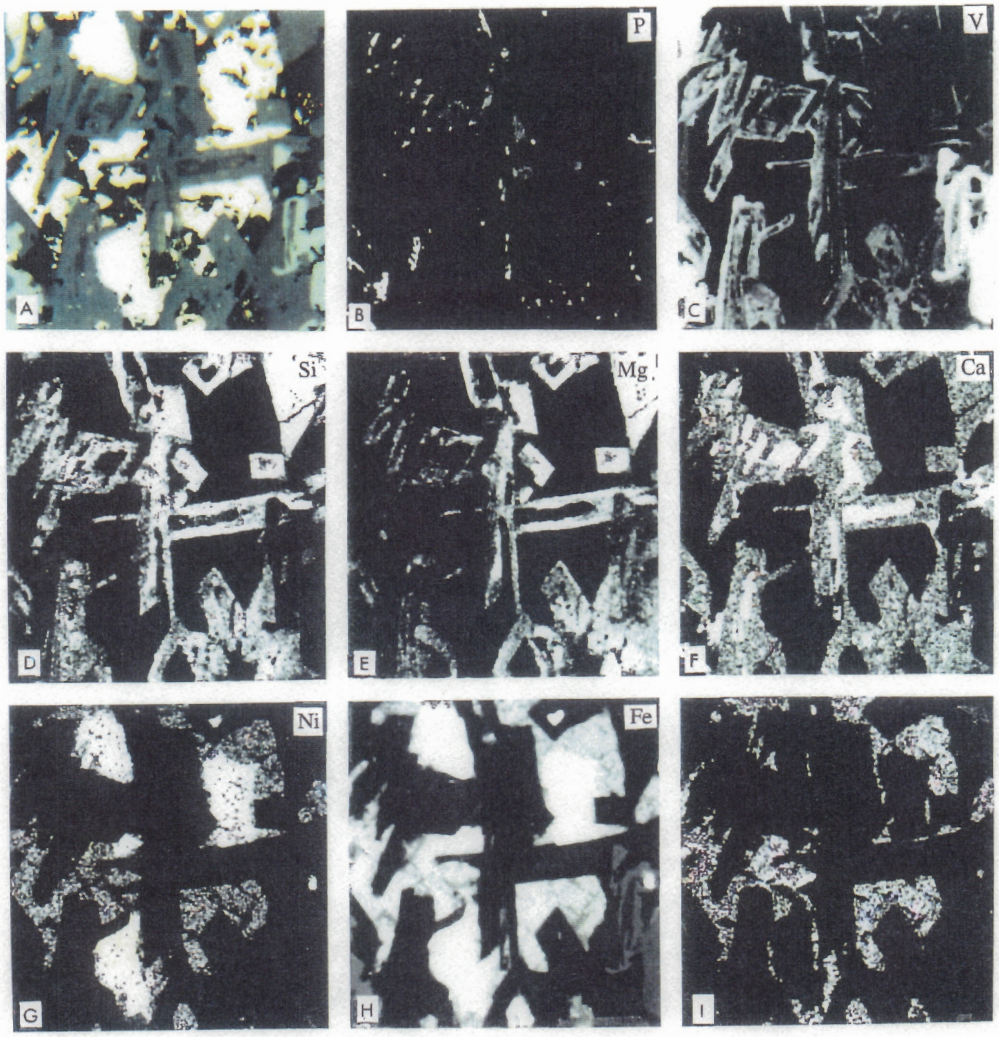

FIG. 4.9. Elemental X-ray maps of the reduced slag region outlined in Fig. 4.8: A) reflected light photomicrograph, B) P distribution, C) V distribution, D) Si distribution, E) Mg distribution, F) Ca distribution, G) Ni distribution, H) Fe distribution, and I) S distribution. Field of view = 160 μm.

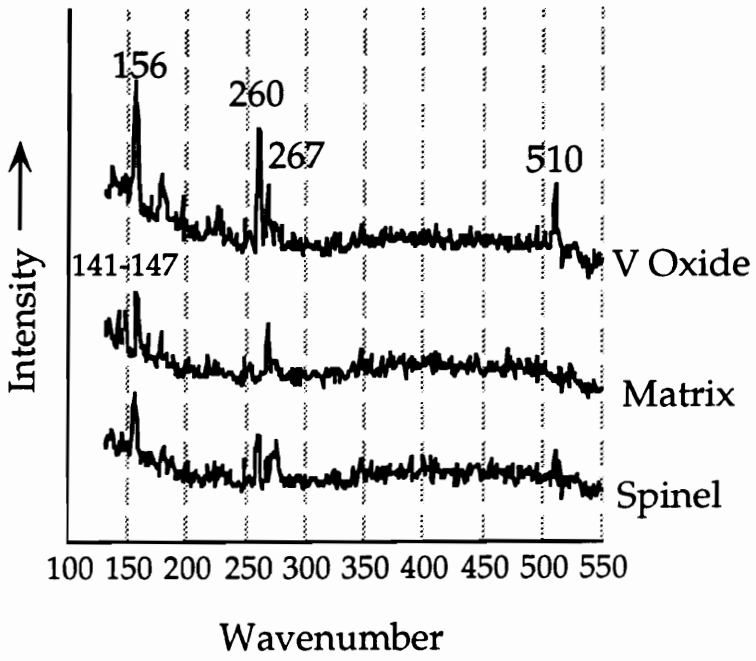

FIG. 4.10. Raman spectra of vanadium-bearing phases in reduced slag samples.

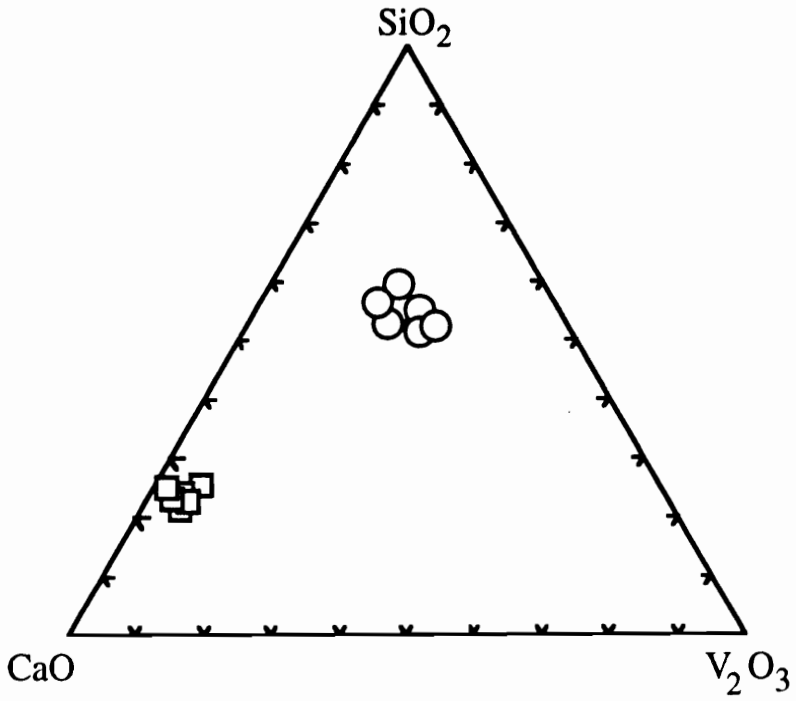

FIG. 4.11. Ternary plot of reduced slag (sample I-4) matrix. Circles represent Ca-silicate, squares represent Ca-oxide.

Table 4.10. Compositional variation of Ca-Silicate matrix in reduced slag (wt. %)

Elemental Weight Percent							Oxide Weight Percent			
Mg	Al	Si	Ca	Fe	V	Σ	SiO_2	CaO	V_2O_3	Σoxides
4.6	5.7	18.3	16.0	3.5	7.4	56.0	45.9	22.5	10.9	103.0
6.5	5.3	18.8	16.9	1.5	5.1	54.5	47.0	23.7	6.9	101.2
6.4	5.8	19.4	16.7	1.7	4.8	55.2	48.7	23.4	6.5	103.1
6.5	5.4	20.2	16.7	1.5	4.7	55.4	50.6	23.3	6.4	102.9

Table 4.11. Compositional variation of Ca-oxide matrix in reduced slag (wt. %). Since no other elements, except for minor P, were detected, it is believed that the low oxide sums reflect either water, carbon or hydrocarbon compounds within the material.

Elemental Weight Percent						Oxide Weight Percent				
Al	Si	Ca	Fe	V	Σ	Al_2O_3	SiO_2	CaO	V_2O_3	Σoxides
0.8	5.8	32.7	0.7	1.1	42.2	1.6	14.6	45.9	1.4	66.5
4.6	4.6	33.1	1.6	0.8	45.3	8.6	11.5	46.4	1.1	71.0
0.4	5.3	33.4	0.6	0.7	41.3	0.8	13.5	46.9	.9	64.2

Fe and Fe-Ni sulfides (Table 4.7) are characteristic of the reduced slags but do not appear in the oxidized slags. Sample I-4 is composed of approximately 20% irregularly shaped sulfide grains that appeared to have formed in interstices around and between the oxide and silicate phases. Sulfides that formed around previously crystallized phases consistently appear to be in the process of consuming the oxide grains (Figure 4.9 G, H, and I). Figure 4.12 shows a sulfide grain that was apparently mantled by VO_2. Note the exsolution lamellae within the Fe-sulfide, and the lower sulfur content of the Fe-Ni sulfide (Fig. 4.12).

Fe-Ni intermetallic compound, of Ni_2Fe composition (Fe:35.2-36.7 wt%; Ni: 65.2-65.4 wt%), makes up approximately 5% of sample I-4. This material is always mantled by sulfide phases, which may have protected them from subsequent oxidation. The lack

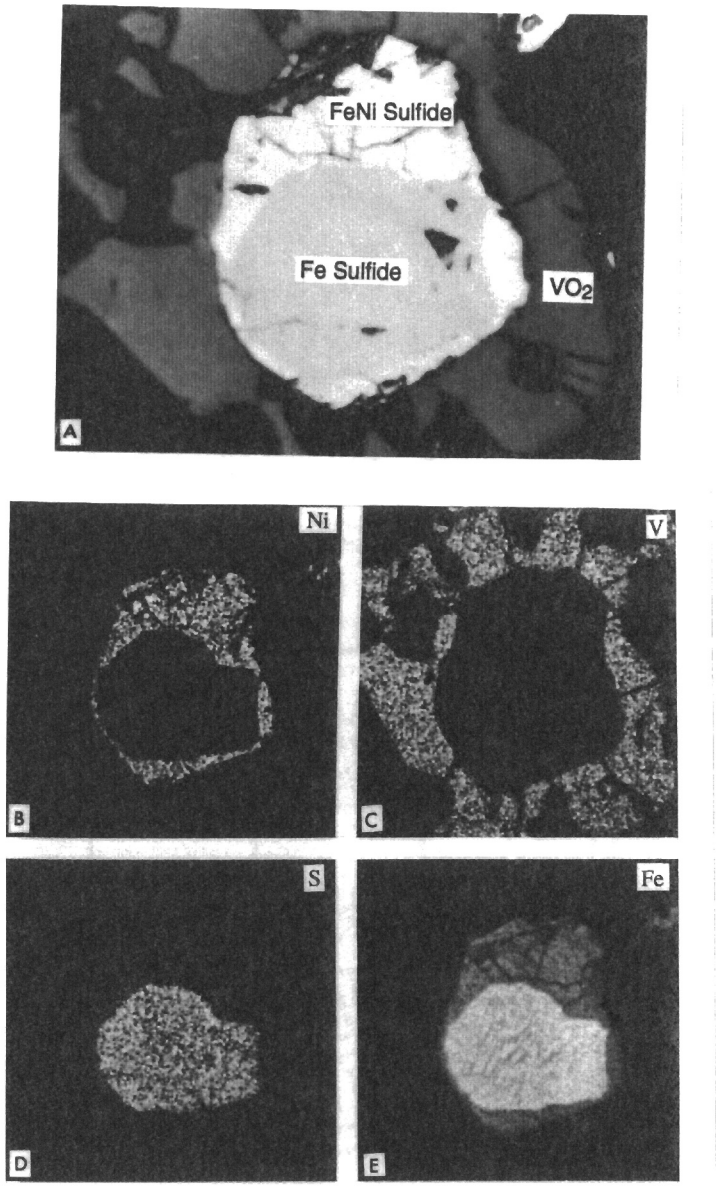

FIG. 4.12. Elemental X-ray maps of a region of reduced slag (sample I-4). Note the exsolution lamellae within the Fe sulfide surrounded by Fe-Ni sulfide, surrounded by VO_2. A) reflected light photomicrograph, B) Ni distribution, C) V distribution, D) S distribution, and E) Fe distribution. Field of view = 100 μm.

of sulfur in this intermetallic compound is evident in that the Fe and Ni rich grains in Figure 4.9G and 4.9H show no sulfur in Figure 4.9I.

The coexisting FeS and Ni_2Fe phases present in the reduced slag (Fig. 4.13) correlate well with experimental results in the Fe-Ni-S system (under reducing conditions) at 650°C, and the coexisting (Fe, Ni)S and Ni_2Fe phases are in equilibrium at 550°C (KULLERUD et al., 1969). These assemblages suggest trapping of the Fe-Ni-S melt at 650°C with subsequent re-equilibration at 550°C, thereby confirming the reduced nature of this material. The absence of Fe-Ni sulfides in the oxidized slag indicates that the addition of oxygen efficiently removes the iron from the structure to form other phases while leaving the nickel to react with the sulfur to form nickel sulfides.

DISCUSSION

Reflected light microscopy in conjunction with electron microprobe analyses readily distinguish the phases present and their abundances within these slags. In non-crystalline material, and in complex phases containing more than one element of variable valence (e.g. V and Fe) exact compositions are not easily ascertained, therefore, an ancillary technique for valence determination was sought. Unfortunately, the phases within these slags are too fine grained for XPS and too poorly crystalline for XRD phase determinations. Raman spectra collected from polished samples in vacuum, at very low temperatures helped determine which vanadium species were present within specific phases containing at least 5 weight % V. Raman analysis is especially sensitive to the presence or absence of V^{+3}, which produces three distinct characteristic peaks. Raman is much less sensitive to V^{+5} and V^{+4}, and is not recommended as a tool for discerning these two valences.

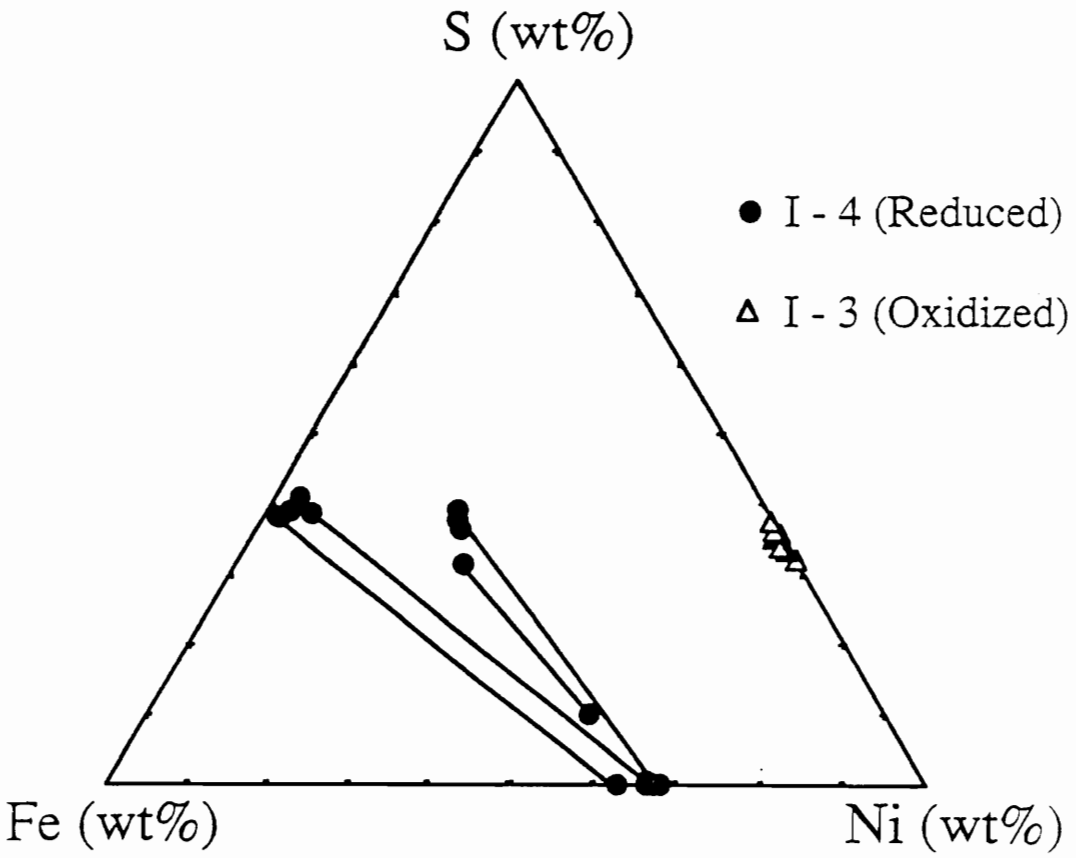

FIG. 4.13. Ternary plot of sulfide and intermetallic compound compositions. Tie lines connect coexisting phases.

The redox conditions present during gasification greatly affect the character of the resultant slag material. Oxidizing conditions produce slags with very poorly crystallized matrices with entrained blebs of an immiscible melt reflecting rapid quenching of molten material, while reducing conditions produce more crystalline matrices presumably produced by a quasi-crystalline, highly viscous slag that was nearly solid upon quenching. The pure vanadium "phenocrysts" present in these slags clearly reflect the redox conditions present during gasification: producing V_2O_5 when oxidized and V_2O_4 when reduced. Redox conditions also greatly affect the composition of the Fe-Ni-S phases in these slags. Oxidizing conditions effectively remove S from the slags, leaving only very minor amounts of Ni sulfide, while reducing conditions produce slags containing much more abundant total sulfides (Fe-Ni sulfides) and Fe-Ni alloys. The spinel compositions are very sensitive to conditions that control the uptake of important elements such as V, Fe and Ni. Although the conditions within the gasifier are too poorly constrained for a complete understanding of spinel formation, different redox conditions appear to produce distinct spinels. Oxidation results in a change in partitioning and the development of two separate spinel types, both of which contain more Ni and Fe and less V than spinels formed under reducing conditions, possibly reflecting the relative overall lack of sulfides in slags formed under oxidizing conditions, and the complete absence of Fe in these sulfides.

These differences can now be applied to other Monte Bello slags in order to estimate conditions within the gasifier. Our results, in tandem with the vast experience of the Texaco engineers may help improve the efficiency of the Texaco petroleum coke gasification system, thereby hastening its large scale implementation.

REFERENCES

CLARK, R.J.K., 1973, Vanadium. In *Comprehensive Inorganic Chemistry* (J.C. Bailor et. al. eds.) **3**, p.491-551, Pergammon Press.

CRAIG, J.R., and NAJJAR, M.S., 1990, Elemental partitioning in coke gasification slags. In *Process Mineralogy IX* (W.Petruk, R.D. Hagni, S. Pignolet-Brandom and D.M. Hausen eds.), p. 485-497, Minerals, Metals and Materials Society, Warrendale, PA.

CRAIG, J.R., NAJJAR, M.S. and ROBIN, A.M., 1990, Characterization of coke gasification slags. In *Process Mineralogy IX* (W.Petruk, R.D. Hagni, S. Pignolet-Brandom and D.M. Hausen eds.), p. 473-483, Minerals, Metals and Materials Society, Warrendale, PA.

CRAIG, J.R. and VAUGHAN, D.J., 1994, *Ore Microscopy and Ore Petrology*, 2nd edition, Wiley Interscience, New York, 435p.

GROEN, J.C., CRAIG, J.R., and NAJJAR, M.S., 1991, Chemical phases in petroleum coke gasification slag. *ACS Div. Fuel Chem. Prepr.* **36**, p. 207-215.

KULLERUD, G., YUND, R.A. and MOH, G.H, 1969, Phase relations in the Cu-Fe-S, Cu-Ni-S, and Fe-Ni-S systems. In *Magmatic Ore Deposits* (H.D.B. Wilson ed.), p. 323-343, The Economic Geology Publishing Co., Lancaster, PA.

VITA

John Ashby Mavrogenes was born on May 14th, 1959 in Aurora, Illinois. He received his bachelors degree in geology from Beloit College, Beloit Wisconsin, in 1983. After working two years as a well site geologist in the Geysers Geothermal Field, California, and two more years as a carpenter, he returned to graduate school and received his masters degree in geology from the University of Missouri-Rolla, Rolla, Missouri in 1989. Following a year at Michigan Tehnological University he transferred to Virginia Polytechnic Institute and State University and completed his PhD in geology in 1994. He currently plans to move to Canberra, Australia for a post doctoral position in experimental geochemistry in the Petrochemistry Group of the Research School of Earth Sciences at the Australian National University.

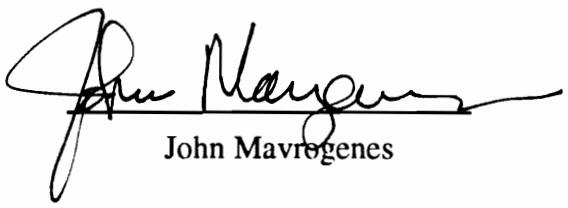

John Mavrogenes